The conserved AAA-ATPase PCH-2 distributes its regulation of meiotic prophase events by remodeling multiple meiotic HORMADs in *C. elegans*

Anna E. Russo*, Stefani Giacopazzi*, Alison Deshong*, Malaika Menon*, Valery Ortiz*, Kaori M. Ego#, Kevin D. Corbett# and Needhi Bhalla*[1]

* Department of Molecular, Cell and Developmental Biology, University of California, Santa Cruz, Santa Cruz, CA 95064

Department of Cellular and Molecular Medicine, University of California, San Diego, La Jolla, CA 92093

[1] corresponding author: nbhalla@ucsc.edu

Department of Molecular, Cell and Developmental Biology

225 Sinsheimer Labs

University of California, Santa Cruz

Santa Cruz, CA 95064

phone: (831) 459-1319

fax: (831) 459-3139

Abstract

During meiotic prophase, the essential events of homolog pairing, synapsis, and recombination are coordinated with meiotic progression to promote fidelity and prevent aneuploidy. The conserved AAA+ ATPase PCH-2 coordinates these events to guarantee crossover assurance and accurate chromosome segregation. How PCH-2 accomplishes this coordination is poorly understood. Here, we provide evidence that PCH-2 decelerates pairing, synapsis and recombination in *C. elegans* by remodeling meiotic HORMADs. We propose that PCH-2 converts the closed versions of these proteins, which drive these meiotic prophase events, to unbuckled conformations, destabilizing interhomolog interactions and delaying meiotic progression. Further, we find that PCH-2 distributes this regulation among three essential meiotic HORMADs in *C. elegans*: PCH-2 acts through HTP-3 to regulate pairing and synapsis, HIM-3 to promote crossover assurance, and HTP-1 to control meiotic progression. In addition to identifying a molecular mechanism for how PCH-2 regulates interhomolog interactions, our results provide a possible explanation for the expansion of the meiotic HORMAD family as a conserved evolutionary feature of meiosis. Taken together, our work demonstrates that PCH-2's remodeling of meiotic HORMADs has functional consequences for the rate and fidelity of homolog pairing, synapsis, recombination and meiotic progression, ensuring accurate meiotic chromosome segregation.

Introduction

All sexually reproducing organisms depend on the specialized cell division called meiosis, which produces haploid gametes such as sperm, eggs, and pollen. During meiosis, cells combine one round of DNA replication with two rounds of chromosome segregation, all of which is tightly regulated to ensure that gametes inherit the correct number of chromosomes. Errors in meiosis can lead to aneuploid gametes that cause infertility, birth defects and miscarriages [1]. Therefore, understanding how meiotic events are coordinated has important implications for reproductive health.

During prophase I of meiosis, chromosome pairs or homologs undergo a series of events known as pairing, synapsis, and crossover recombination. First, homologs find each other and pair within the nucleus. Next, a molecular structure called the synaptonemal complex (SC) assembles between homologs and stabilizes homolog pairing in a process called synapsis. Finally, homologs undergo crossover recombination, which serves two important purposes. First, it shuffles alleles to create new genetic combinations that can be acted upon by natural selection. Second, it physically links homolog pairs, which is required for homologs to properly remodel, orient on the spindle, and segregate correctly during the first meiotic division.

Despite being described as a linear pathway, the processes of pairing, synapsis and recombination between homologous chromosomes are highly dynamic and can occur simultaneously, requiring active coordination. Further, these events can also initiate inappropriately between non-homologous chromosomes and therefore need to be corrected. We have shown that the highly conserved AAA+ ATPase, Pachytene checkpoint 2 (PCH-2), contributes to both the coordination and correction of meiotic events [2, 3]. However, how it carries out these roles is currently unclear.

PCH-2, and its mammalian ortholog TRIP13, has been shown to act through a family of proteins that contain a HORMA domain (HORMAD proteins) to mediate a variety of chromosome behaviors, including meiotic interhomolog interactions. HORMADs were named after the first proteins in this family to be discovered in budding yeast: Hop1, Rev7, and Mad2 [4] and meiotic HORMADs are essential to organize meiotic chromosomes for the meiosis-specific events of homolog pairing, synapsis, and recombination [5]. Despite having essential roles in meiotic prophase, meiotic HORMADs differ greatly across eukaryotes in the number of family members they contain. For example, *S. cerevisiae* and *S. pombe* each have one meiotic HORMAD [6, 7], mice and *Arabidopsis* have two [8-10] and *C. elegans* has four [11-14]. In both mice and plants, one meiotic HORMAD plays a more integral role in the events of pairing, synapsis, and recombination than the other, indicating some specialization of function [9, 10, 15-18]. This specialization is also observed in *C. elegans* among the three essential HORMADs [19]. HTP-3 is responsible for DNA double-strand break formation [12] and REC-8-mediated sister chromatid cohesion [20]. HIM-3 promotes synapsis [19] and homolog access to ensure repair off the homolog versus the sister chromatid during crossover recombination [21]. HTP-1, in addition to contributing to homolog access along with HIM-3, also controls the timely initiation of SC assembly once homologs are paired properly [11, 13] and the protection of sister chromatid cohesion during the first meiotic division [22]. The fourth meiotic HORMAD, HTP-2, is not essential and is largely redundant with HTP-1 [13, 22].

Meiotic HORMAD proteins have a characteristic N-terminal HORMA domain that allows HORMADs to adopt two different conformations: a closed conformation and an open/unlocked conformation (reviewed in [23]). In the closed conformation, a peptide on a binding partner called the “closure motif” binds the core of the HORMAD’s HORMA domain. This interaction is stabilized by a C-terminal region of the HORMA domain called the safety belt, which wraps around the HORMAD to lock the binding partner’s closure motif against the HORMA domain

core. Conversion of the HORMAD from the closed to open conformation occurs when the PCH-2/TRIP13 binds and partially unfolds the extreme N-terminus of the HORMA domain, resulting in a structural rearrangement that releases the bound closure motif and causes the safety belt to occupy the closure motif interaction site. Biochemical and structural studies show that PCH-2/TRIP13 is directly responsible for the conversion of closed conformers to open conformers for the mitotic HORMADs Mad2 [24] and Rev7 [25], where this remodeling relies on a direct interaction between PCH-2/TRIP13 and the N-terminus of the HORMAD [26, 27].

Conformational switching has also been shown to be essential for meiotic HORMAD function. Closed versions of meiotic HORMADs assemble on meiotic chromosomes to drive pairing, synapsis, recombination, and meiotic progression [19]. While stable, open conformers of meiotic HORMADs have not been observed *in vitro* or *in vivo*, the budding yeast meiotic HORMAD, Hop1, exists in solution as two distinct conformations that are in equilibrium: the closed conformation and an intermediate “extended” state that has been referred to as unbuckled [28]. The physiological relevance of unbuckled meiotic HORMADs *in vivo* is unclear but work in plants and budding yeast indicates that their unbuckling is required for nuclear import and association with meiotic chromosomes [29, 30].

While studies with other HORMADs, such as Mad2 and Rev7, provide a powerful framework to conceptualize PCH-2’s molecular mechanism during meiotic prophase, identifying PCH-2’s specific role during meiosis has been challenging. In contrast to Mad2 and Rev7, attempts to undertake similar structural and biochemical analysis of PCH-2/TRIP13 and meiotic HORMADs have been less informative. However, prior evidence from budding yeast, plants, and mammals indicates that PCH-2/TRIP13 binds and acts directly on meiotic HORMADs. In budding yeast, Pch2 has been shown to bind to and remodel meiotic HORMADs *in vitro* [31]. Additionally, PCH-2’s orthologs in other systems have been shown to promote meiotic progression [32] by

depleting or redistributing meiotic HORMADs from chromosome axes upon synapsis, including budding yeast [33, 34], *Arabidopsis* [35] and mice [10]. In mice, the removal of the meiotic HORMAD, HORMAD1, at the onset of synapsis is abolished in both TRIP13 mutants [10] or when the N-terminus of HORMAD1 is deleted [27], indicating that PCH-2 and its orthologs' remodeling of meiotic HORMADs is similar to its remodeling of Mad2 and Rev7. However, in some systems, such as *C. elegans*, meiotic HORMADs do not rely on PCH-2 for nuclear import [2] nor are they removed from chromosomes upon synapsis [21, 22, 36]. Further, PCH-2 and its orthologs localize to meiotic chromosomes as foci prior to synapsis in budding yeast, plants and *C. elegans* [2, 34, 35, 37, 38] and meiotic HORMADs are not fully removed during synapsis in budding yeast, plants or mice [10, 33, 35]. These data raise the important question of whether remodeling of meiotic HORMADs plays additional roles during meiotic prophase.

Here, we use a combination of genetic, cytological and biochemical data to demonstrate that PCH-2 remodels meiotic HORMADs to regulate and coordinate pairing, synapsis, crossover recombination, and meiotic progression in *C. elegans*. We show that a missense mutation in the HORMA domain of HTP-3 suppresses pairing and synapsis defects in *pch-2* mutants but exacerbates its recombination defects, indicating these two proteins cooperate to promote pairing and synapsis but regulate recombination independently. We also show that a similar mutation in *him-3* exacerbates synapsis defects in *pch-2* mutants but suppresses its recombination defects, suggesting that PCH-2 acts on HIM-3 specifically to promote crossover recombination. Finally, we show that corresponding mutations in the meiotic HORMAD HTP-1 produce a delay in meiotic progression, with consequences for synapsis and recombination, and can be partially suppressed by a mutation in *pch-2*, suggesting that PCH-2 cooperates with HTP-1 to regulate meiotic progression. Biochemical analysis demonstrates that these mutations limit the ability of meiotic HORMADs to adopt their closed conformations. Taken together, our work strongly supports a model in which PCH-2's remodeling of meiotic HORMADs from closed

to unbuckled conformations decelerates pairing, synapsis, recombination, and meiotic progression, to proofread homolog interactions and maintain meiotic fidelity. Further, PCH-2 cleanly delegates its regulation of different meiotic prophase events to different meiotic HORMADs, offering new insight into how PCH-2 mechanistically coordinates the events of pairing, synapsis, and recombination. Lastly, it provides a potential explanation for why this family of meiotic HORMADs has dramatically expanded in *C. elegans* and provides a possible explanation about why some model systems have multiple meiotic HORMADs.

Results

PCH-2's localization is consistent with remodeling HORMADs on the axial elements of meiotic chromosomes

Meiotic HORMADs collaborate with cohesins and other axial proteins to organize meiotic chromosomes into linear axial elements functionally capable of undergoing interhomolog pairing, synapsis and recombination [5]. While PCH-2/TRIP13 has been implicated in remodeling meiotic HORMADs away from meiotic chromosomes to ensure their availability [29, 39] and entry into the nucleus [30], its localization to meiotic chromosomes before and after synapsis [2, 34, 35, 37, 38] suggests a role remodeling meiotic HORMADs on chromosomes to regulate pairing, synapsis and recombination as well as meiotic progression. To test this, we used structured illumination microscopy to more closely investigate whether PCH-2's localization was consistent with remodeling meiotic HORMADs on axial elements.

Before synapsis and during axis assembly, when meiotic HORMADs are diffuse throughout nuclei, PCH-2 localizes to foci on meiotic chromosomes [2]. After synapsis, PCH-2 localizes along the synaptonemal complex (SC) and this localization depends on the central element component SYP-1 [2, 40], which assembles between axial elements during synapsis (Figure

1A). We performed indirect immunofluorescence on wildtype meiotic nuclei against both PCH-2 and SYP-1 and performed structured illumination microscopy to resolve the distance between axial elements (Figure 1B) [41]. While SYP-1 appeared as a line of continuous width in all meiotic nuclei, PCH-2 staining often appeared wider than SYP-1, sometimes splitting as parallel tracks with SYP-1 staining between PCH-2 tracks (inset and arrows in Figure 1B, Figure 1C). Indeed, when we quantified the signal intensities for both PCH-2 and SYP-1, we found that the signal for PCH-2 spanned a wider distance compared to SYP-1 (Figure 1D), indicating that PCH-2 can reside on or close to axial elements of synapsed chromosomes and remodel meiotic HORMADs on chromosomes.

htp-3 ^{H96Y} suppresses the acceleration of pairing and synapsis in *pch-2* mutants

Having established that PCH-2's localization is consistent with the ability to remodel meiotic HORMADs on meiotic chromosomes, we looked for genetic interactions that might support this possibility. *htp-3(vc75)* is a missense mutation that replaces histidine 96 with a tyrosine in the HORMA domain (H96Y) (Figure 2A). HTP-3^{H96Y} properly localizes to meiotic chromosomes [42] and does not affect pairing, synapsis and crossover recombination [42, 43]. However, we and others previously showed that this mutation in *htp-3* abolished meiotic checkpoint responses in *C. elegans* [42, 43]. Because of this phenotype, we analyzed HTP-3's relationship with PCH-2 in regulating pairing, synapsis, recombination, and meiotic progression.

To test whether PCH-2 genetically interacts with HTP-3 to regulate pairing, we generated *pch-2;syp-1* double mutants, *htp-3*^{H96Y}*;syp-1* double mutants, and *pch-2;htp-3*^{H96Y}*;syp-1* triple mutants and assessed pairing when compared with *syp-1* single mutants. *syp*-1 null mutants successfully undergo pairing despite the failure to load SC components, particularly at specific loci called Pairing Centers (PCs) [40]. Therefore, these experiments allow us to analyze pairing independent of synapsis. We performed immunofluorescence against the HIM-8 protein, which

localizes to PCs on the X chromosome [44], to assess pairing at this locus throughout the germline: two HIM-8 foci indicate the X-chromosomes are unpaired while a single HIM-8 focus indicates paired X-chromosomes. Because meiotic nuclei are arranged in spatiotemporal gradient in germlines, we divided the germline into six equivalently sized zones to perform a meiotic time-course and determined the percentage of nuclei with a single HIM-8 focus in each zone (Figure 3A and 3B).

Similar to previous work [2, 3], we found that there is an increase in percentage of nuclei with paired X chromosomes in zone 2 for *pch-2;syp-1* double mutants (76%, Figure 3C) compared to *syp-1* single mutant controls (49%, Figure 3C), showing that the rate of pairing is accelerated in the absence of *pch-2* (p value <0.0001 by two-tailed Fisher's exact test). *htp-3*^{H96Y}*;syp-1* double mutants have a similar rate of pairing compared to *syp-1* single mutant controls (46%, Figure 3C, p value = 0.4001 by two-tailed Fisher's exact test), demonstrating that this mutation does not affect the rate of pairing. Interestingly, we found that *pch-2;htp-3*^{H96Y}*;syp-1* triple mutants have a similar rate of pairing compared to *syp-1* single mutants and *htp-3*^{H96Y}*;syp-1* double mutants (49%, Figure 3C), indicating that *htp-3*^{H96Y} suppresses the acceleration of pairing observed in *pch-2* mutants.

Next, we tested for a genetic interaction between *pch-2* and *htp-3* during synapsis. We analyzed the rate of synapsis in germlines from control, *pch-2* single mutants, *htp-3*^{H96Y} single mutants, and *pch-2;htp-3*^{H96Y} double mutant worms by performing immunofluorescence against the axial element HTP-3 [12, 36] and the central element SYP-1 [40]. We then determined the fraction of nuclei with complete synapsis in each zone. Complete synapsis is visible as full co-localization of HTP-3 and SYP-1, whereas nuclei with incomplete synapsis have stretches of HTP-3 without SYP-1 signal (arrowheads, Figure 3D). Similar to previous data, we report that *pch-2* null mutants have an accelerated rate of synapsis (61%, Figure 3E) compared to wildtype controls

(32%, Figure 3E, p value <0.0001 by two-tailed Fisher's exact test) in zone 2 and a delay in desynapsis in zone 6 [2, 3] (Figure 3E). *htp-3*^{H96Y} single mutants have a similar rate of synapsis compared to wildtype controls (36%, Figure 3E, p value = 0.228 by two-tailed Fisher's exact test), suggesting that the rate of synapsis is unaffected in this background, and accelerated desynapsis, as previously reported [42]. Analogous to our pairing results, we found that *pch-2;htp-3*^{H96Y} double mutants have a similar rate of synapsis compared to wildtype controls and *htp-3*^{H96Y} single mutants (34%, Figure 3E), indicating that *htp-3*^{H96Y} suppresses the acceleration of synapsis in *pch-2* mutants.

To further solidify that PCH-2 acts on HTP-3 to regulate synapsis, we analyzed synapsis in *meDf2* heterozygotes (*meDf2/+*). *meDf2* is a mutation in which PC regions are deleted from the X chromosome [45]. Since PCs are essential for pairing and synapsis [36], *meDf2* homozygotes fail to pair and synapse X chromosomes while *meDf2* heterozygotes behave like a partial loss of function mutation: ~50% of nuclei complete synapsis of X chromosomes while the remaining 50% have unsynapsed X chromosomes [36]. In *pch-2;meDf2/+* worms, ~85% of nuclei complete synapsis, demonstrating that PCH-2 normally inhibits synapsis when PC function is compromised [2].

To test whether *htp-3*^{H96Y} also suppressed the synapsis in *pch-2;meDf2/+* worms, we generated *pch-2;htp-3*^{H96Y}*;meDf2/+* triple mutants and analyzed the rate of synapsis, comparing it to controls. Similar to previous results, we found that 87% of nuclei in *pch-2;meDf2/+* double mutants achieve complete synapsis in zone 5 compared to 48% complete synapsis for *meDf2/+* single mutant worms (Figure 3F). *htp-3*^{H96Y}*;meDf2/+* worms have 52% of nuclei with complete synapsis in zone 5, similar to *meDf2/+* single mutants (Figure 3F). *pch-2;htp-3*^{H96Y}*;meDf2/+* triple mutants show maximal levels of synapsis in zone 4 (36%, Figure 3F) and more closely resemble the levels of synapsis observed in to *htp-3*^{H96Y}*;meDf2/+* double and *meDf2/+* single

mutants than *pch-2;meDf2/+* double mutants. These data indicate that PCH-2's ability to inhibit synapsis when PC function is compromised depends on the function of HTP-3, and perhaps more specifically, on the HORMA domain of HTP-3, similar to what we observed when PCs are fully functional (Figure 3E). To determine whether these defects in synapsis produce chromosome segregation errors, we scored the percent of male progeny in these strains. Male progeny, which are genotypically XO in contrast to XX hermaphrodites, are diagnostic of misegregation of X chromosomes in meiosis. The ability of *htp-3*^{H96Y} to suppress the synapsis of X chromosomes in *pch-2;meDf2/+* was further supported by the increase in male progeny observed in *pch-2;htp-3*^{H96Y}*;meDf2/+* triple mutants (10.84%, Table 1) in comparison to *pch-2;meDf2/+* double mutants (0.83%, Table 1).

htp-3^{H96Y} exacerbates defects in DNA repair and crossover formation in *pch-2* mutants

We next tested whether PCH-2 regulates recombination through HTP-3 by assaying DNA repair and crossover formation in *pch-2;htp-3*^{H96Y} double mutants. The rate of DNA repair is assessed by quantifying the number of RAD-51 foci per nucleus throughout the germline (Figure 3G). The appearance of RAD-51 foci on meiotic chromosomes is associated with the introduction of DNA double-strand breaks and their disappearance is associated with the entry of DNA double-strand breaks into repair pathways [46]. RAD-51 numbers peak in zone 4 in wildtype animals, increasing to an average of 2 per nuclei, and decrease as RAD-51 is removed during DNA repair. *pch-2* single mutants have a lower average of RAD-51 foci per nucleus in zones 4-6 (Figure 3H), consistent with previous findings that that *pch-2* mutants exhibit a faster rate of DNA repair compared to wildtype controls [2]. *htp-3*^{H96Y} single mutants show a similar rate of DNA repair as wildtype germlines (Figure 3H), although the average number of RAD-51 foci is slightly lower than wildtype [42]. By contrast, *pch-2;htp-3*^{H96Y} double mutants not only show an accelerated rate of DNA repair, similar to *pch-2* single mutants, they have a reduced average number of RAD-51 foci in zone 5 (0.75 foci, Figure 3H), showing that mutation of *htp-3*

exacerbates the acceleration of DNA repair in *pch-2* mutants. Because *htp-3*^{H96Y} and *pch-2* mutants do not have reduced numbers of DNA double-stranded breaks [2, 42], these results reflect changes in the rate of DNA repair. Further, this indicates that, in contrast to our findings for pairing and synapsis, PCH-2 does not act through HTP-3 to regulate the rate of DNA repair. Instead, both proteins regulate DNA repair independent of each other.

We previously reported that *pch-2;htp-3*^{H96Y} double mutants exhibit more achiasmate chromosomes than either single mutant [2], indicating that the double mutant has a more severe defect in meiotic crossover recombination than either single mutant and consistent with our analysis of DNA repair (Figure 3H). To further verify this result on crossover formation, we quantified the number of GFP::COSA-1 foci for each meiotic nucleus. COSA-1 is a cyclin-like protein that localizes specifically to presumptive crossovers, serving as a cytological marker for crossover formation [47]. Because *C. elegans* contain 6 pairs of chromosomes and exhibit strong crossover interference, most wildtype nuclei have 6 GFP::COSA-1 foci per nucleus (Figure 3I) [47]. Our findings also reflect this, where we report only 3% of nuclei have less than 6 GFP::COSA-1 foci (Figure 3J). We also found that the incidence of nuclei with less than 6 GFP::COSA-1 foci increases to 9% of nuclei in *pch-2* single mutants (Figure 3J, p value < 0.0001 by Fisher's exact test), recapitulating previous findings that *pch-2* mutants exhibit a loss of crossover assurance [2, 3]. *htp-3*^{H96Y} single mutants also show an increase in the number of nuclei with less than 6 GFP::COSA-1 crossovers compared to wildtype (7%, Figure 3J, p value = 0.003 by Fisher's exact test), consistent with their checkpoint role [42]. Similar to our analysis of DNA repair, the number of nuclei with less than 6 GFP::COSA-1 foci in *pch-2;htp-3*^{H96Y} double mutants increases to 11% percent (Figure 3J, p value <0.0001 by Fisher's exact test), showing an additive effect for crossover defects. These data illustrate that PCH-2 and HTP-3 work independently to regulate crossover formation.

Altogether, our analysis of pairing, synapsis and crossover recombination indicate that PCH-2 and HTP-3 act together to regulate pairing and synapsis but independently to regulate DNA repair and crossover formation. Since *htp-3*^{H96Y} single mutants also show defects in the DNA damage response [43] while *pch-2* mutants do not [48], this separation of function is not necessarily surprising. However, more importantly these data strongly support a model in which PCH-2 acts through HTP-3's HORMA domain to control the rate of pairing and synapsis but not the process of meiotic recombination.

htp-3^{H96Y} does not affect meiotic progression

In budding yeast, Pch2's remodeling of the meiotic HORMAD, Hop1, contributes to meiotic progression [32]. Since *htp-3*^{H96Y} mutants genetically interact with *pch-2* mutants in *C. elegans*, we also tested whether *htp-3*^{H96Y} mutants affected meiotic progression. We assessed meiotic progression by performing immunofluorescence against a factor required for DNA double-strand break formation, DSB-1 (Figure S1A). DSB-1 localizes to meiotic chromosomes to facilitate DNA double-strand break formation [49]. In response to meiotic defects, DSB-1 persists on chromosomes to maintain a period of competency for DNA double-strand break formation to promote crossover assurance [49] and this persistence correlates with other markers of delays in meiotic progression [50, 51]. We quantified the fraction of meiotic nuclei that were positive for DSB-1 and could not detect any difference between control and *htp-3*^{H96Y} mutant germlines (Figure S1B, p value = 0.8269 by Fisher's exact test), illustrating that this mutation does not affect meiotic progression.

A null mutation in *htp-3* abolishes the delay in meiotic progression observed when there are defects in synapsis, such as in *syp-1* mutants [50]. To determine whether *htp-3*^{H96Y} affected meiotic progression in *syp-1* mutants, we quantified the fraction of DSB-1 positive meiotic nuclei in both *syp-1* single mutants and *syp-1;htp-3*^{H96Y} double mutants and could not observe any

difference between these genotypes (Figure S1C, p value = 1.0 by Fisher's exact test), indicating that *htp-3*^{H96Y} does not affect the extension of meiotic progression observed when there are meiotic defects.

him-3^{R93Y} does not suppress the acceleration of pairing or synapsis in *pch-2* mutants

Our findings that PCH-2 acts on HTP-3 to promote pairing and synapsis, but not recombination, indicates that PCH-2 regulates recombination through an HTP-3 independent mechanism. Further, it is unclear whether PCH-2 regulates pairing and synapsis only through its interaction with HTP-3 or whether other meiotic HORMADs also contribute to this regulation. To address these possibilities, we next tested whether *pch-2* genetically interacts with similar mutations in *him-3* or *htp-1*, genes that encode the two other HORMADs essential for meiosis in *C. elegans*.

We performed a Clustal Omega alignment of HTP-3 with the other three meiotic HORMADs [52] and observed that the mutation in *htp-3*^{H96Y} was not of a conserved residue but was adjacent to two invariant residues in all four meiotic HORMADs (red box in Figure 2B). Further, based on this alignment, the arginine at position 93 of HIM-3 should be positioned similarly within the HORMA domain (Figures 2C and D). Using CRISPR/Cas9 gene editing, we made a corresponding missense mutation to the *htp-3*^{H96Y} allele in *him*-3, where arginine 93 was replaced with a tyrosine (*him-3*^{R93Y}). Indirect immunofluorescence verified that this mutation did not affect HIM-3's localization to chromosomes (Figure S2), progeny viability or the production of male progeny (Table 1).

First we analyzed pairing in *syp-1*, *pch-2;syp-1*, *him-3*^{R93Y}*;syp-1*, and *pch-2;him-3*^{R93Y}*;syp-1* mutants by performing immunofluorescence against HIM-8 (Figure 4A and 4B). *him-3*^{R93Y}*;syp-1* double mutants show 44% of nuclei completed pairing in zone 2, similar to *syp-1* single mutants (p value =1.00 by two-tailed Fisher's exact test), demonstrating that this mutation does not

affect pairing (Figure 4B). In contrast to our analysis of the *htp-3*^{H96Y} allele, we found that *pch-2;him-3*^{R93Y}*;syp-1* triple mutants also show an accelerated rate of pairing phenotype (63%, Figure 4B) similar to that of *pch-2;syp-1* double mutants (p value = 0.52 by two-tailed Fisher's exact test). Therefore, we detect no genetic interaction between *pch-2* and *him-3*^{R93Y} in affecting the rate of pairing.

Next, we assessed the rate of synapsis in wildtype, *pch-2*, *him-3*^{R93Y}, and *pch-2;him-3*^{R93Y} germlines by performing immunofluorescence against SYP-1 and HTP-3 (Figure 4C and 4D). In both *pch-2* and *him-3*^{R93Y} single mutants, we found that there was an increase in the number of nuclei that completed synapsis in zone 2 (13% for both, compared to the wildtype control of 3%, Figure 4D), suggesting that synapsis is accelerated in both mutants (p values <0.0001 for both comparisons by two-tailed Fisher's exact test). However, we found that *pch-2;him-3*^{R93Y} double mutants display more severe synapsis defects than either single mutant: the rate of synapsis is delayed throughout zones 2-5 and these double mutants reach only 87% complete synapsis throughout the germline (Figure 4D). These results demonstrate that PCH-2 and HIM-3 regulate the progression of synapsis independent of each other.

Finally, we further assessed synapsis in *him-3*^{R93Y} *and pch-2;him-3*^{R93Y} mutants by scoring synapsis in *meDf2* heterozygotes (*meDf2/+*). Consistent with a role in regulating synapsis, *him-3*^{R93Y}*;meDf2/+* double mutants show a reduced rate of synapsis (Figure 4E) compared to *meDf2/+* controls (see zones 4 and 5). This effect was intermediate in *pch-2;him-3*^{R93Y};*meDf2/+* triple mutant worms, providing further support that PCH-2 and HIM-3 both regulate synapsis but accomplish this through independent mechanisms.

<u>*him-3*^{R93Y} does not suppress DNA repair defects in *pch-2* mutants</u>

We next tested whether *pch-2* genetically interacts with *him-3*^{R93Y} during the regulation of DNA repair by scoring RAD-51 foci in N2, *pch-2*, *him-3*^{R93Y} and *pch-2;him-3*^{R93Y} mutants (Figure 4F). In *him-3*^{R93Y} single mutants, the average number of RAD-51 foci was higher in zone 3 than both *pch-2* and control germlines, suggesting a more rapid installation of RAD-51 and potentially more DNA double-strand breaks. However, the rate of DNA repair was similar to wildtype (Figure 4G). *pch-2*;*him-3*^{R93Y} worms more closely resembled *him-3*^{R93Y} single mutants than *pch-2* single mutants in zone 3 but was intermediate between *him-3*^{R93Y} and *pch-2* single mutants in zone 4 (Figure 4G), indicating that the accelerated rate of DNA repair observed in *pch-2* mutants is not fully suppressed by the *him-3*^{R93Y} mutation and that these two factors do not act in the same pathway to regulate DNA repair.

him-3^{R93Y} suppresses crossover recombination defects in *pch-2* mutants

To analyze the effect of *him-3*^{R93Y} on crossover recombination, and test for a genetic interaction with *pch-2* mutants, we scored GFP::COSA-1 foci in wildtype, *pch-2, him-3*^{R93Y} and *pch-2;him-3*^{R93Y} mutant strains (Figure 4H). Similar to *pch-2* single mutants, we found that there was an increase of nuclei with less than 6 GFP::COSA-1 foci in *him-3*^{R93Y} mutants compared to wildtype controls (10%, Figure 4I, p value = 0.0004 by two-tailed Fisher's exact test), showing that mutation of this residue in HIM-3 causes a loss of crossover assurance. In contrast to *pch-2* mutants and *him-3*^{R93Y} single mutants, *pch-2;him-3*^{R93Y} double mutants have a reduced number of nuclei with less than 6 foci compared to either single mutant and more closely resembles the frequency observed in wildtype nuclei (5%, Figure 4I, p values = 0.016 and 0.0214 by two-tailed Fisher's exact test, respectively). Therefore, *him-3*^{R93Y} suppresses the defect on crossover assurance observed in *pch-2* mutants.

We next visualized whether we could observe this genetic suppression later in meiotic prophase, when chromosome pairs are linked by chiasmata. Wildtype *C. elegans* oocytes

contain 6 pairs of chromosomes or bivalents, and these can be visualized as 6 “DAPI stained bodies”. Defects in recombination produce homologs without chiasmata, or univalents, in oocytes (arrows, Figure 4J). In our analysis of wildtype oocytes, we did not observe any univalents (Figure 4K). Similar to our previous findings [2], we found that there was an increase in the percent of nuclei with univalents in *pch-2* single mutants compared to wildtype controls (0.8%, Figure 4K), further demonstrating a loss of crossover assurance that leads to achiasmate homolog pairs. Correlating with our GFP::COSA-1 analysis, *him-3*^{R93Y} single mutants also have an increase in the number of oocytes containing univalents (1.3%, Figure 4K), demonstrating that *him-3*^{R93Y} mutants also observe a loss of crossover assurance. In *pch-2;him-3*^{R93Y} double mutants, we found no instances of univalents (Figure 4K), further indicating that these two mutant alleles genetically suppress each other in the context of crossover recombination.

Taken together, our results are consistent with a model in which PCH-2 acts through HIM-3 to promote crossover recombination but not pairing or synapsis. Further, the roles of the two meiotic HORMADs appear to be cleanly delegated, with PCH-2 controlling pairing and synapsis through HTP-3 and crossover recombination through HIM-3. Since we do not observe a similar genetic interaction when we analyze DNA repair in *pch-2;him-3*^{R93Y} double mutants, this regulation of crossover recombination occurs later than the installation and removal of RAD-51.

him-3^{R93Y} does not affect meiotic progression

We next tested whether *him-3*^{R93Y} mutants affect meiotic progression by performing immunofluorescence against DSB-1 and quantifying the fraction that were DSB-1 positive in wildtype and *him-3*^{R93Y}mutant strains (Figure S3A). We found that there was not a significant difference between the number of DSB-1 positive nuclei between wildtype and *him-3*^{R93Y} mutant strains (Figure S3B, p value =0.645 blank by two-tailed Fisher’s exact test), suggesting that this mutation does not affect meiotic progression.

We further tested whether the *him-3*^{R93Y} mutation affected meiotic progression by quantifying the fraction of DSB-1 positive nuclei in *syp-1* and *him-3*^{R93Y}*;syp-1* mutant strains. Similar to our findings for *htp-3*^{H96Y}, we found that there was not a significant difference in the number of DSB-1 positive nuclei between *syp-1* single mutants and *him-3*^{R93Y}*;syp-1* double mutants (Figure S3C, p value =1.00 by two-tailed Fisher's exact test). This result further demonstrates that *him-3*^{R93Y} does not affect meiotic progression.

<u>*htp-1*^{G97T} does not suppress the accelerated rate of pairing in *pch-2* mutants</u>

Our findings suggest that PCH-2 acts through HTP-3 to promote pairing and synapsis, and HIM-3 to promote crossover formation. We next wanted to test whether *pch-2* genetically interacts with a similar mutation in *htp-1*, the gene that encodes the final essential meiotic HORMAD in *C. elegans*.

Preliminary structural analysis of the HORMA domain of HTP-1 indicates that the glycine residue that is analogous to the histidine and arginine residues of HTP-3 and HIM-3 (Figure 2B), respectively, is positioned more internally within the HORMA domain (Figure 2E) and therefore potentially more constrained in the mutations we can introduce at this site without affecting HTP-1's stability. Indeed, when we replaced this glycine with a tyrosine by CRISPR/Cas9 gene editing (*htp-1*^{G97Y}), this mutant phenotypically resembled the *htp-1*(*me84)* null allele [11] in which this glycine residue is mutated to a glutamate, producing very few viable progeny and a high incidence of male (HIM) phenotype. Given that the severity of the *htp-1*^{G97Y} mutation would preclude our analysis of meiotic prophase events, we sought to create a less severe hypomorphic allele of HTP-1 to test whether it genetically interacts with the *pch-2* null mutation.

To identify a mutation that would allow analysis of pairing, synapsis, recombination, and meiotic progression, we used CRISPR/Cas9 to substitute glycine 97 with amino acids that progressively add bulkier side chains at this position (*htp-1*^{G97A}, *htp-1*^{G97S}*, and htp-1*^{G97T}). Upon initial examination of these strains, we observed a HIM phenotype associated with the *htp-1*^{G97T} mutant strain (Table 1), suggesting that this mutation causes meiotic chromosome misegregation. This HIM phenotype was accompanied by a reduction in embryonic viability (Table 1). Therefore, we limited our analysis of testing genetic interactions with *pch-2* for pairing, synapsis, and recombination to *htp-1*^{G97T} mutants. Indirect immunofluorescence showed no difference in the loading of HTP-1 to meiotic chromosomes in *htp-1*^{G97T} mutants or in *htp-1*^{G97T} *htp-2* double mutants (Figure S4).

We first tested whether pairing is disrupted in this strain by performing immunofluorescence against HIM-8 in *syp-1*, *pch-2;syp-1*, *htp-1*^{G97T};*syp-1* and *pch-2*;*htp-1*^{G97T};*syp-1* mutant germlines (Figure 5A and 5B). In *htp-1*^{G97T};*syp-1* double mutants, the percent of nuclei that have completed pairing in zone 2 is similar compared to *syp-1* single mutants (Figure 5B, p value =0.553 by two-tailed Fisher's exact test), indicating that *htp-1*^{G97T};*syp-1* double mutants do not have a defect in the progression of pairing. *pch-2;htp-1*^{G97T};*syp-1* triple mutants have a similar rate of pairing in zone 2 compared to *pch-2;syp-1* double mutants (Figure 5B, p value =0.311 by two-tailed Fisher's exact test), showing that the *htp-1*^{G97T} mutation does not suppress the acceleration of pairing observed in *pch-2* mutants.

<u>*htp-1*^{G97T} causes severe synapsis defects that are not suppressed by mutation of *pch*-2</u>

Next, we tested whether synapsis is perturbed in *htp-1*^{G97T} mutants and whether this allele genetically interacts with the *pch-2* null allele (Figure 5C and 5D). Synapsis is severely disrupted in *htp-1*^{G97T} mutants: despite some chromosomes completing synapsis (Figure 5D),

almost all meiotic nuclei have some number of unsynapsed chromosomes throughout the germline, where only 1.3% of nuclei reach complete synapsis (Figure 5D). In *pch-2*;*htp-1*^{G97T} double mutants, we find that synapsis is disrupted as severely as *htp-1*^{G97T} single mutants, where 1.3% of nuclei also reach complete synapsis (Figure 5D, p value =0.717 by two-tailed Fisher's exact test), indicating that these alleles do not genetically interact and regulate synapsis independent of each other.

htp-1^{G97T} leads to a delay in RAD-51 removal that is not suppressed by mutation of *pch-2*

Next, we assessed the progress of DNA repair in *htp-1*^{G97T} and *pch-2*;*htp-1*^{G97T} mutants by scoring RAD-51 foci throughout the germline (Figure 5E and 5F). In comparison to control germlines, *htp-1*^{G97T} single mutants exhibit a delay in the installation of RAD-51 foci (Figure 5F). However, as meiotic prophase continues, meiotic nuclei in *htp-1*^{G97T} single mutants have more RAD-51 foci and substantially delay their removal, possibly as an indirect consequence of the defects in synapsis we observe in this mutant (Figure 5D). *pch-2*;*htp-1*^{G97T} double mutants no longer exhibit this delay in RAD-51 installation, suggesting a partial suppression of this particular phenotype, but display more RAD-51 foci, particularly in zones 4 and 5, than wildtype meiotic nuclei and *pch-2* single mutants, similar to *htp-1*^{G97T} single mutants. Thus, PCH-2 and HTP-1 do not appear to genetically interact to regulate the rate of DNA repair.

htp-1^{G97T} causes defects in crossover recombination that are not suppressed by *pch-2* mutations

To continue our analysis, we analyzed crossover recombination by scoring the number of GFP::COSA-1 foci per nucleus in wildtype, *pch-2*, *htp-1*^{G97T}, and *pch-2*;*htp-1*^{G97T} mutants (Figure 5G and 5H). Surprisingly, we found that in *htp-1*^{G97T} single mutants, the number of COSA-1 foci

varies greatly across nuclei, ranging from 4 to 9, with only 39% of nuclei have 6 GFP::COSA-1 foci (Figure 5H), suggesting that the *htp-1*^{G97T} mutation causes misregulation of crossover formation. In addition to the loss of crossover assurance (nuclei with less than 6 GFP::COSA-1 foci), we also observe a loss of crossover interference (nuclei with greater than 6 GFP::COSA-1 foci), indicating a general loss of crossover control in *htp-1*^{G97T} mutants. In *pch-2*;*htp-1*^{G97T} double mutants, we observe a similar phenotype where the number of GFP::COSA-1 varies across nuclei, ranging from 4 to 9, with only 45% having 6 COSA-1 foci (Figure 5H, p value =0.1725 by two-tailed Fisher's exact test). Overall, these data indicate that PCH-2 and HTP-1 do not genetically interact to regulate crossover recombination.

We further analyzed crossover formation by looking directly at bivalents in oocytes and quantified the frequency of univalents in wildtype, *pch-2*, *htp-1*^{G97T}, and *pch-2*;*htp-1*^{G97T} mutants (Figure 5I and 5J). In *htp-1*^{G97T} single mutants, we found that the frequency of univalents significantly increases to 41% (Figure 5J, p value < 0.0001 by two-tailed Fisher's exact test), further verifying the defect in crossover formation in *htp-1*^{G97T} single mutants. For *pch-2*;*htp-1*^{G97T} double mutants, we also found that the frequency of univalents is statistically higher compared to wildtype oocytes (31%,Figure 5J, p value < 0.0001 by two-tailed Fisher's exact test) but not significantly different when compared to *htp-1*^{G97T} single mutants (31%, Figure 5J, p value =0.182 by two-tailed Fisher's exact test). Taken together, this suggests that both *pch-2* and *htp-1* both promote crossover assurance but regulate it through different mechanisms.

<u>*htp-1*^{G97T} delays meiotic progression and this delay is partially suppressed by mutation of *pch-2*</u>

The absence of HTP-1 accelerates meiotic progression, producing non-homologous synapsis and more rapid DNA repair [11]. In contrast, mutations within the HORMA domain of HTP-1 that prevent its loading on meiotic chromosomes cause a delay in meiotic progression, producing

asynapsis [53]. We tested whether *htp-1*^{G97T} mutations similarly affect meiotic progression by performing immunostaining against DSB-1.

We quantified the fraction of DSB-1 positive meiotic nuclei in wildtype and *htp-1*^{G97T} mutant germlines (Figure 6A). We found that *htp-1*^{G97T} mutants display a statistically significant increase in the fraction of DSB-1 positive nuclei (81%, p value < 0.0001 by two-tailed Fisher's exact test Figure 6B), indicating that this mutation produces a delay in meiotic progression. Since DSB-1 is required for DNA double-strand break formation, the extension of DSB-1 likely explains the increase in RAD-51 foci (Figure 5F) and the attenuation of crossover interference (Figure 5H) in *htp-1*^{G97T} mutants. Moreover, since the increase in RAD-51 foci formation (Figure 5F) is accompanied by an increase in GFP::COSA-1 foci (Figure 5H), *htp-1*^{G97T} mutants also appear to have defects in crossover homeostasis, a mechanism that ensures that the number of crossovers remain invariant even when the number of crossover precursors, such as DNA double-strand breaks, vary [54] and which is particularly robust in *C. elegans* [47].

Given the severity of this phenotype, we wondered if the less severe mutations we generated, *htp-1*^{G97A} and *htp-1*^{G97S} mutants, might also affect meiotic progression, albeit more weakly (Figure 6A). While *htp-1*^{G97A} mutants did not affect the fraction of DSB-1 positive nuclei, *htp-1*^{G97S} mutants produced a small but statistically significant delay in meiotic progression (63% DSB-1 positive nuclei, Figure 6B, p value =0.0006 by two-tailed Fisher's exact test), indicating that the introduction of bulkier amino acids at this residue produces an allelic series with respect to defects in meiotic progression.

We next tested whether this defect in meiotic progression in *htp-1*^{G97T} single mutants is suppressed by the *pch-2* mutation. We found that the percent of DSB-1 stained nuclei is slightly but significantly lower in *pch-2*;*htp-1*^{G97T} double mutants (77%, Figure 6B) compared to *htp-1*^{G97T}

single mutants (Figure 6B, p value = 0.0047 by two-tailed Fisher's exact test), indicating that the meiotic progression defect in *htp-1*^{G97T} mutants is partially suppressed by mutations in *pch-2* and that these two proteins cooperate to regulate meiotic progression.

him-3^{R93Y} and *htp-1*^{G97T} mutants have functional meiotic checkpoints

We previously showed that *htp-3*^{H96Y} mutants abolishes both the DNA damage response and the synapsis checkpoint [43], similar to null mutations in *htp-3* and *him-3* [55]. A null mutation in *htp-1* only affects the synapsis checkpoint [55]. To determine whether *him-3*^{R93Y} or *htp-1*^{G97T} mutants affect meiotic checkpoint activation, we introduced each mutation into the *syp-1* mutant background and evaluated the levels of germline apoptosis. *syp-1* mutants activate both the DNA damage response and the synapsis checkpoint, producing high levels of germline apoptosis [48]. *him-3*^{R93Y} mutants showed wildtype levels of apoptosis while *htp-1*^{G97T} mutants exhibited germline apoptosis similar to that of *syp-1* single mutants (Figure S6, p value < 0.0001 by student t-test), likely as a consequence of the asynapsis and defects in recombination we observe (Figure 5). Both *syp-1;him-3*^{R93Y} and *syp-1;htp-1*^{G97T} double mutants showed similar levels of germline apoptosis as *syp-1* single mutants (Figure S6), indicating that both *him-3*^{R93Y} or *htp-1*^{G97T} mutants are competent for meiotic checkpoint activation, unlike *htp-3*^{H96Y} mutants [43].

him-3^{R93Y} mutants maintain the structure of the HORMA domain but have reduced affinity for closure motifs

Our data thus far demonstrates that *pch-2* genetically interacts with specific alleles of *htp-3*, *him-3* and *htp-1*, with varying effects on pairing, synapsis, recombination and meiotic progression. However, how these genetic interactions translate into a molecular understanding

of the functional relationship between PCH-2 and these meiotic HORMADs is unclear. To address this, we tested what effect these mutations had on the ability of meiotic HORMADs to bind their closure motifs and adopt the closed conformation.

While the closure motif for HTP-3 is unknown, HIM-3 is known to bind closure motifs found within the C-terminal tail of HTP-3 [19]. HIM-3 also contains a closure motif in its own C-terminus but it preferentially binds closure motifs in HTP-3 to contribute to a hierarchical HORMAD assembly [19]. We cloned and expressed wildtype HIM-3 and HIM-3^{R93Y} in *E. coli*, purified each protein, and performed a fluorescence polarization peptide binding assay to test how well HIM-3^{R93Y} binds a peptide encoding HTP-3 closure motif #4 *in vitro*. Consistent with prior work, we found that wildtype HIM-3 binds the HTP-3 closure motif with a K_d of 220 +/- 20 nM and found that it does not bind to a control peptide with a scrambled sequence (Figure 7A). HIM-3^{R93Y} binds to the same closure motif with an increased K_d of 690 +/- 130 nM, indicating that HIM-3^{R93Y} binds the HTP-3 closure motif with reduced affinity compared to wildtype HIM-3 (Figure 7A). The thermal stability of HIM-3^{R93Y} is similar to that of wild-type HIM-3 (Figure S5), and a crystal structure of HIM-3^{R93Y} in the closed conformation is equivalent to that of wildtype HIM-3 (Figure 2D), suggesting that reduced affinity for the closure motif for HIM-3^{R93Y} is not due to instability of the protein or an inability to adopt the closed conformation. These results demonstrate that HIM-3^{R93Y} binds the HTP-3 closure motif less readily than wildtype HIM-3, which would potentially limit its ability to adopt the closed conformation *in vivo* (Figure 7B). Because this residue is positioned similarly within all three-essential meiotic HORMADs (Figure 2B), our biochemical analysis of HIM-3^{R93Y} may be generalizable to the mutant versions of HTP-3 and HTP-1: HTP-3^{H96Y} and HTP-1^{G97T} could bind their respective closure motifs with less affinity, affecting their ability to adopt the closed conformation *in vivo*.

Unlike the budding yeast meiotic HORMAD, Hop1 [56], HIM-3 is difficult to purify in any conformation aside from its closed conformation [19], preventing us from directly assessing whether the HIM-3^{R93Y} mutation affects the protein's closed-versus-unbuckled conformational equilibrium. However, the reduced affinity of HIM-3^{R93Y} for the HTP-3 closure motif, when combined with the established conformational dynamics of Hop1 [56], the localization of PCH-2 by structured illumination microscopy (Figure 1) and our genetic and cytological analysis (Figures 3-6) of how these mutant alleles suppress some defects observed in *pch-2* mutants, presents a model consistent with PCH-2 remodeling meiotic HORMADs from a closed to unbuckled conformation on meiotic chromosomes to control the progress of pairing, synapsis, meiotic recombination and cell cycle progression (Figure 8).

Discussion

Since the discovery of Pch2 in budding yeast more than 20 years ago, the particular roles of Pch2/PCH-2/TRIP13 in meiosis have been enigmatic. More recently, biochemical and structural analysis of how mammalian TRIP13 contributes to spindle checkpoint progression by remodeling the HORMA domain protein MAD2 have provided a useful framework to establish Pch2/PCH-2/TRIP13's diverse roles in structuring meiotic chromosomes for homolog pairing, synapsis, and recombination, and signaling meiotic progression. In the spindle checkpoint, PCH-2/TRIP13 promotes checkpoint activation by maintaining a pool of soluble "open" MAD2, which is used to build the mitotic checkpoint complex at unattached kinetochores and delay anaphase onset [57-59]. After kinetochore attachment, TRIP13 plays an additional role in human cells, disassembling the mitotic checkpoint complex by remodeling MAD2, promoting checkpoint inactivation and anaphase progression [60, 61]. This activity may not necessarily be conserved, given that a similar role in silencing the checkpoint is not observed in *C. elegans* [59, 62], and Pch2 is not expressed outside meiosis in *S. cerevisiae* [38]. Nonetheless, in some

systems, TRIP13 appears to play dual roles in spindle checkpoint activation and inactivation, through a single biochemical activity of converting “closed” MAD2 to the “open” conformer.

Recently, studies of Pch2 in budding yeast, and by extension plants and mammals, have suggested that this enzyme plays a similar dual role in meiotic chromosome organization, homologous recombination, and meiotic progression. Meiotic HORMADs in most organisms adopt a “self-closed” conformation with their HORMA domains bound to a closure motif in their own C-terminus [19, 28, 30]. In budding yeast and plants, Pch2/TRIP13’s remodeling activity is needed to convert these “self-closed” HORMADs into an “open” or “unbuckled” conformation to promote their nuclear import and association with chromosomes [29, 30]. After assembly into axial elements of meiotic chromosomes, HORMADs promote meiotic recombination and homolog pairing [6, 63], likely through direct protein-protein interactions with partner proteins [23]. Once homologs have recombined and synapsed, Pch2/TRIP13 is recruited to the synaptonemal complex [34, 35, 38], where it is thought to disassemble HORMAD-axis protein complexes to deplete them [10, 33, 35]. HORMAD depletion down-regulates recombination, promotes rapid repair of remaining DNA breaks, and facilitates meiotic progression [64, 65].

In *C. elegans*, several key differences in the timing of meiotic events relative to yeast, plants, and mammals necessitate a rethinking of PCH-2’s roles in meiotic progression. First, homolog pairing and synapsis occur independently of recombination in *C. elegans* [66], such that synapsis cannot serve as a signal for successful interhomolog recombination as in other organisms. Second, meiotic HORMADs localize to meiotic chromosomes independently of PCH-2 [2] and are not visibly depleted in response to synapsis [21, 22, 36], indicating the dual role for Pch2/TRIP13 proposed in other systems is not relevant to understanding PCH-2’s function in *C. elegans* meiosis. Finally, a null mutation of *pch-2* or mutations that eliminate its ATP hydrolysis activity result in accelerated homolog pairing, synapsis, and meiotic

recombination, leading to a loss of meiotic fidelity [2, 3]. Because these events are likely mediated by direct HORMAD-partner protein interactions on meiotic chromosomes, and because PCH-2 is localized to chromosomes during the relevant stages of meiotic prophase (Figure 1) [2], these phenotypes suggest that PCH-2 either reduces overall levels of HORMADs or increases their association-dissociation dynamics to modulate these key events.

Our experiments from this study shed further light on this model. We have identified mutations in the HORMA domains of both HTP-3 and HIM-3 (Figure 2A) that appear to load normally on chromosomes [42] (Figures S2 and S4), reduce the affinity of closure motif interactions in vitro (Figure 7) and suppress specific defects of a *pch-2* null mutation in homolog pairing/synapsis and recombination, respectively (Figures 3 and 4). These data lead us to propose a model in which PCH-2 remodels the HORMA domains of chromosome-associated HORMADs from the "closed" conformation to the "open/unbuckled" conformation to temporarily reduce HORMAD occupancy on chromosomes, decelerating HORMAD-dependent homolog pairing, synapsis, and recombination to promote meiotic fidelity (Figure 8). An attractive but still speculative extension to this model is that PCH-2's remodeling of meiotic HORMADs destabilizes HORMAD-partner protein interactions essential for homolog pairing, synapsis, and recombination, deliberately slowing their progress.

Our model has important implications for the established roles of Pch2/TRIP13 in other organisms. First, Pch2/PCH2 in both yeast and plants localize specifically to sites associated with synapsis initiation and recombination [34, 35], suggesting a similar role temporarily reducing HORMAD occupancy at these sites prior to synapsis. Further, despite the observation that Pch2/TRIP13 strongly depletes meiotic HORMADs from chromosomes upon synapsis, these proteins are not completely removed from chromosomes in any organism [10, 33, 35], suggesting roles for both meiotic HORMADs and Pch2/TRIP13 even after chromosome

synapsis. Given that the gradual implementation of crossover formation partially overlaps when chromosomes are synapsed in budding yeast, plants, and mice [67-70], we propose that the presence of Pch2/TRIP13 on synapsed chromosomes remodels meiotic HORMADS to regulate the number and location of crossovers, similar to one role of PCH-2 in *C. elegans* [2, 71].

The relationship between PCH-2 and HTP-1 is less clear. Despite the small structural differences between HIM-3 and HTP-1 (Figure 2E) that required some adjustments in how we designed our mutational analysis of HTP-1, we predict that HTP-1^{G97T} also shows a reduced affinity for its closure motifs in both HTP-3 and HIM-3, potentially shifting its equilibrium toward the unbuckled conformation. The consequences of this difference in protein function are a significant delay in meiotic progression (Figure 6B) and defects in synapsis, DNA repair and crossover recombination (Figure 5D, 5F, & 5H). Since previous data has implicated HTP-1 and its regulation in controlling meiotic progression, with indirect effects on synapsis, DNA repair and crossover recombination [11, 53, 72] , we favor the interpretation that the primary defect in *htp-1^{G97T}* mutants is the delay in meiotic progression, with secondary, indirect consequences for synapsis and recombination. Mutation of *pch-2* partially suppresses this defect in meiotic progression (Figure 6B), with little effect on synapsis or recombination (Figure 5D & 5H), supporting our interpretation. How might a delay in meiotic progression prevent complete synapsis or the normal completion of recombination? This meiotic delay might maintain a cell cycle state in which the synaptonemal complex and/or recombination intermediates are more labile and subject to turnover, through mechanisms such as post-translational modifications, high chromosome mobility, some other unknown condition or some combination of these conditions. Finally, if we are correct and an increase in unbuckled HTP-1^{G97T} is responsible for a meiotic delay, with indirect consequences on synapsis and recombination, our data also suggest that, unlike open MAD2, unbuckled versions of meiotic HORMADs may have additional

functions aside from being an important structural intermediate poised for binding to closure motifs in partner proteins.

That mutation of *pch-2* only weakly suppresses the delay in meiotic progression we observe in *htp-1*^{G97T} mutants raises two possibilities: 1) the *htp-1*^{G97T} mutation is too severe to allow us to observe this genetic interaction; or 2) PCH-2 does not directly act on HTP-1 to regulate meiotic progression. How might PCH-2 contribute to the regulation of meiotic progression without directly remodeling HTP-1? Since both HTP-3 and HIM-3 have HTP-1 closure motifs in their C-termini [19], PCH-2's remodeling of HTP-3 and HIM-3 may indirectly result in the removal, and remodeling, of HTP-1, contributing to the regulation of meiotic progression. This possibility is particularly attractive since it explicitly coordinates meiotic progression with the rate of pairing, synapsis and recombination.

Finally, our work shows that PCH-2's regulation of pairing, synapsis, recombination and meiotic progression are cleanly delegated to the remodeling of different meiotic HORMADs: PCH-2 remodels HTP-3 from a closed to an unbluckled conformation to decelerate pairing and synapsis and contribute to checkpoint activation, HIM-3 to decelerate crossover recombination and HTP-1, either directly or indirectly, to control meiotic progression. This deceleration allows for proofreading of the homolog interactions that underlie these events and ensure fidelity [3]. Similar separation of function has been observed in plants and mice: each have two meiotic HORMADs, only one of which (HORMAD1 in mice, ASY1 in plants), appears to be essential for pairing, synapsis and recombination [9, 15-17, 73]. In the case of mice, a second HORMAD, HORMAD2, is not required for pairing, synapsis or recombination but is essential for efficient meiotic checkpoint responses [18, 74]. In plants, no role for ASY2 has been reported yet. The separation of function we observe in *C. elegans* is slightly different: The three essential meiotic HORMADs have overlapping but distinct roles that nonetheless significantly impact pairing,

synapsis and recombination [11-13, 19, 21, 22]. However, it is through their regulation by PCH-2 that their distinct roles become more clear, allowing for the coordination of pairing, synapsis, recombination and meiotic progression. This delegation of tasks, as revealed by their regulation by PCH-2, may also explain why this family has expanded so dramatically in *C. elegans*. Since multiple systems, including mammals, also have more than one meiotic HORMAD, this delegation of tasks may be a conserved evolutionary feature of meiosis.

Another possible contributing factor to the expansion of this family in *C. elegans* is the mechanistic uncoupling of meiotic recombination with synapsis. Mice, budding yeast and plants all rely on the initiation of meiotic recombination [75-78] to promote accurate synapsis. Similarly, all of these organisms have a single essential meiotic HORMAD controlling pairing, synapsis and recombination [6, 9, 15], suggesting a possible connection between these observations. In contrast to these systems, *C. elegans* does not rely on meiotic recombination for accurate chromosome synapsis [66], suggesting that the family of meiotic HORMADs may have expanded to accommodate the fact that synapsis and recombination are regulated by two different mechanisms in this system.

While *C. elegans* is unique in that it has four meiotic HORMADs which assemble into a hierarchical complex, it is formally possible that other systems also have different functional classes of meiotic HORMADs, even when they have a single meiotic HORMAD in their genome. For example, in budding yeast, Hop1 can bind directly to nucleosomal DNA [79], a closure motif in the axis protein Red1 and closure motifs in Hop1 once it has bound to Red1, producing oligomerization [28]. These three different classes of Hop1, potentially defined by the molecular nature of their binding to meiotic chromosomes, may also assemble hierarchically and have different effects on the events of meiotic prophase. These differences could affect their regulation by Pch2, producing a similar delegation of functions as we observe with HTP-3, HIM-

3 and HTP-1. For example, it has already been shown in budding yeast that in regions adjacent to telomeres, Hop1 is resistant to Pch2-mediated redistribution [80], consistent with this possibility of differential regulation by Pch2.

Our data show that the remodeling of meiotic HORMADs by PCH-2 have consequences on the progress, coordination, and fidelity of meiotic prophase events. Major questions that arise from this work are 1) how is PCH-2 activity limited to meiotic HORMADs in some contexts but not others and 2) how do these meiotic HORMADs contribute to the events of pairing, synapsis and crossover recombination? How does HTP-3 molecularly participate in pairing and synapsis? How does HIM-3 promote crossover recombination? And how does HTP-1 control meiotic progression? Future studies focused on understanding how meiotic HORMADs molecularly interact with each other, other axis proteins, and/or additional binding partners will shed new light on how meiotic HORMADs, in collaboration with PCH-2, drive the coordination of meiotic prophase events to promote fidelity and prevent aneuploidy.

Materials and Methods

Genetics, Worm strains

The C*. elegans* Bristol N2 strain was used as the wildtype strain throughout this study [81]. All strains were grown at 20°C under standard conditions unless otherwise stated. Mutations and rearrangements used were as follows:

LG I: *htp-3(vc75), mnDp66*

LG II: *pch-2(tm1458), meIs8 [Ppie-1::GFP::cosa-1 + unc-119(+)]*

LG IV: *him-3(blt9), htp-1(blt10), htp-1(blt11), htp-1(blt12), htp-2(tm2543)*, *nT1[unc-?(n754let-?(m435)]*

LG V: *syp-1(me17), bcIs39[Plim-7::ced-1::gfp; lin-15(+)]*

LG X: *meDf2*

The *him-3*^{R93Y} (*him-3[blt9]), htp-1*^{G97A} (*htp-1[blt10])*, *htp-1*^{G97S} (*htp-1[blt11]),* and *htp-1*^{G97T} (*htp-1[blt12])* were generated by CRISPR-Cas9 genome editing supplemented with the *dpy-10* co-conversion method [82].

The following guide RNA sequences were used:

dpy-10 sgRNA: 5'GCU ACC AUA GGC ACC ACG AGG UUU UAG AGC UAU GCU 3'

him-3 sgRNA: 5'CGU GUG UCU UCA ACA UUC GAG UUU UAG AGC UAU GCU 3'

htp-1 sgRNA: 5' UCA ACU ACU UCG AAA UGC UGG UUU UAG AGC UAU GCU 3'

The following DNA repair oligonucleotide sequences were used:

dpy-10: 5' CAC TTG AAC TTC AAT ACG GCA AGA TGA GAA TGA CTG GAA ACC GTA CCG CAT GCG GTG CCT ATG GTA GCG GAG CTT CAC ATG GCT TCA GAC CAA CAG CCT AT 3'

him-3^{R93Y}: 5' GCA TTC CAG AGC AGT GTT CCT GCC GCA AAG CGT GTG TCT TCA ACA TTT GAC GGA TTG TAC GAT GCG ATT CAA CAA GGC TAT TTG CGA GAG TTC GCA ATC GTG TTC TAC AAG 3'

htp-1^{G97A}: 5' GCT TCA GAA ACC CAC GGT CTA ACC AAA TCG CTC AAC TAC TTC GAA ATG CTG CTG ATG CAA CAA AGG ATG GGT TTC TGA AAG AAG TCT CCC TCG TGA TCA CAA ATA ATG 3'

htp-1^{G97S}: 5' GCT TCA GAA ACC CAC GGT CTA ACC AAA TCG CTC AAC TAC TTC GAA ATG CTT CAG ATG CAA CAA AGG ATG GGT TTC TGA AAG AAG TCT CCC TCG TGA TCA CAA ATA ATG 3'

htp-1 ^{G97T}: 5' 5' GCT TCA GAA ACC CAC GGT CTA ACC AAA TCG CTC AAC TAC TTC GAA ATG CTA CAG ATG CAA CAA AGG ATG GGT TTC TGA AAG AAG TCT CCC TCG TGA TCA CAA ATA ATG 3'

For CRISPR/Cas9 gene editing, all mutations were made in the N2 wildtype strain, with the exception of the *htp-1*^{G97T} *htp-2* double mutant strain, in which the *htp-1*^{G97T} mutation was introduced in the *htp-2(tm2543)* mutant background. sgRNAs and oligo repair templates were synthesized by Integrated DNA technologies (IDT, Coraville, IA). Injection mixes contained either *htp-1* or *him-3* sgRNA (100 µM final), *dpy-10* sgRNA (100 µM final, [82]), tracrRNA (100 µM final, IDT), purified Cas9 protein (40 µM final), *htp-1* or *him-3* DNA repair oligo (50 µM final, IDT) and *dpy-10* repair oligo (50 µM final, IDT, [82]). Young adults were injected, recovered and stored at either 15 or 20 degrees. Roller or *dpy* F1's were singled to individual plates seeded with OP50 and screened for presence of the mutant allele by PCR and BspHI restriction digest (*htp-1)* or RsaI restriction digest (*him-3*). Individual F2's were then isolated from F1 plates that contained the allele to identify a homozygous strain.

All mutations were verified by sequencing and strains were backcrossed against wildtype worms three times.

Immunofluorescence, Antibodies and Microscopy

Day 1 adult hermaphrodites were dissected 24-28 hours post-late L4 stage and immunostaining and DAPI staining were performed similarly to [48]. For analyzing bivalents, hermaphrodites were dissected and DAPI stained 48 hours post late L4 stage.

The following primary antibodies were used for this study: rat anti-HIM-8 1:500 [44], guinea pig anti-HTP-3 1:250 [36], chicken anti-HTP-3 1:250 [36], rabbit anti-SYP-1 1:500 [40], guinea pig anti-SYP-1 1:500 [40], rabbit anti-HIM-3 1:500 [14], rabbit anti-HTP-1 1:400 [22], rabbit anti-RAD-51 1:250 (Novus Biologicals, Littleton, CO), guinea pig anti-DSB-1 1:250 [49], mouse anti-GFP 1:100 (Invitrogen, Waltham, MA) and rabbit anti-PCH-2 1:500 [2].

The following secondaries were used for this study: Alexa 488 anti-guinea pig (Invitrogen), Alexa 488 anti-rabbit (Invitrogen), Alexa 488 anti-mouse (Invitrogen), Cy3 anti-rabbit (Jackson Immunochemicals, West Grove, PA), Cy3 anti-rat (Jackson Immunochemicals), Cy3 anti-guinea pig (Jackson Immunochemicals), and Cy5 anti-chicken (Jackson Immunochemicals). All secondary antibodies were used at a 1:500 dilution.

To visualize meiotic nuclei and bivalents, DAPI was used at a dilution of 1:10,000.

For analysis of the rate of paining, “paired” nuclei were scored as a single focus, whether it was elongated or circular. “Unpaired” nuclei were scored as two completely separate foci that each had an individual border.

For analysis of the rate of synapsis, nuclei were considered “completely synapsed” when complete colocalization of HTP-3 and SYP-1 was observed. “Unsynapsed” nuclei were assigned when nuclei had stretched of HTP-3 with missing SYP-1 signal.

Scoring of germline apoptosis was performed as previously described in [48] in strains containing *bcIs39 [lim-7p::ced-1::GFP + lin-15(+)]* with the following exceptions: L4 hermaphrodites were allowed to age for 22-24 hours. They were then mounted under coverslips on 2% agarose pads containing 0.2mM levamisole and scored. A minimum of twenty-five germlines was analyzed for each genotype.

Line scans measuring pixel intensity for Figure 1D were performed in ImageJ. Channels were split and the pixel intensities for each fluorophore was measured across the distance of the region of interest (Figure 1C, yellow line). Distance in pixels and normalized intensity were plotted using R (R core team) with the ggplot2 package [83].

All images except for those in Figure 1 were acquired using a DeltaVision Personal DV system (Applied Precision) equipped with a 100X N.A. 1.40 oil-immersion objective (Olympus), resulting in an effective XY pixel spacing of 0.064 or 0.040 µm. Three-dimensional image stacks were collected at 0.2-µm Z-spacing and processed by constrained, iterative deconvolution. For structured Illumination microscopy, images were obtained as 125 nm spaced Z stacks, using a 100x NA 1.40 objective on a DeltaVison OMX Blaze microscopy system, 3D-reconstructed and corrected for registration using SoftWoRx. Image scaling and analysis were performed using functions in the softWoRx software package. Projections were calculated by a maximum intensity algorithm. Composite images were assembled and some false coloring was performed with ImageJ.

Whole germline images were assembled in ImageJ as in [84] using pairwise stitching and/or grid collection stitching [85]. Quantification of pairing, synapsis, RAD-51 foci, GFP::COSA-1 foci, and DSB-1 positive nuclei was performed as in [3] with a minimum of three germlines per genotype.

Protein Expression and Purification

The full-length HIM-3 gene (residues 2-291) was PCR-amplified from a *C. elegans* cDNA library and cloned into UC Berkeley Macrolab vector 2-CT (Addgene #29706), which encodes a TEV protease-cleavable His_6-MBP (maltose binding protein) tag. PCR-based mutagenesis was used to generate the R93Y mutant construct. Proteins were expressed in *E. coli* strain Rosetta2 pLysS (EMD Millipore) at 20°C for 16 hours, then harvested by centrifugation. Proteins were purified using Ni^{2+} affinity chromatography (HisTrap HP, Cytiva), followed by TEV protease treatment [86] for 48 hours. The cleaved mixture was passed through Ni^{2+} affinity resin a second time to remove uncleaved protein, free His_6-MBP tags, and His_6-tagged TEV protease, and the flow-through was concentrated and further purified by size exclusion chromatography (Superdex 200; Cytiva). Fractions were concentrated by ultrafiltration (Amicon Ultra, EMD Millipore), aliquoted, and stored at -80°C.

Fluorescence polarization binding assays

N-terminal FITC-Ahx labeled peptides were synthesized (BioMatik), resuspended in DMSO, then diluted into binding buffer (20 mM Tris pH 7.5, 300 mM NaCl, 10% glycerol, 1 mM DTT, 0.1% NP-40). Fifty µL reactions containing 50 nM peptide plus indicated amounts of HIM-3 (WT or R93Y) protein were incubated 60 minutes at room temperature, then fluorescence polarization was read in 384-well plates using a TECAN Infinite M1000 PRO fluorescence plate reader. All binding curves were done in triplicate. Binding data were analyzed with Graphpad Prism v. 8 using a single-site binding model.

ThermoFluor assays

For protein stability measurement by ThermoFluor assay, purified proteins were diluted to 0.1 mg/mL in a buffer containing 20 mM Tris-HCl pH 7.5, 300 mM NaCl, 10% glycerol, and 1 mM DTT. 0.5 μL of SPYRO Orange dye (5,000X concentrate; Thermo Fisher Scientific #S6650) was mixed with 49.5 μL protein solution, and the mixture was sealed in an optically clear PCR plate. In a Bio-Rad CFX Connect real-time PCR system, fluorescence was measured in scan mode "FRET" during a 25°-99° temperature ramp (0.5° intervals, 30 second hold per interval). For analysis, the change in fluorescence per step was plotted against temperature, and the peak of this plot (the representing the inflection point in the upward slope of the raw fluorescence curve) was taken as the melting temperature (Tm).

Protein crystallization and structure determination

For crystallization, HIM-3(R93Y) was concentrated to 15-20 mg/mL in crystallization buffer (20 mM HEPES pH 7.5, 100 mM NaCl, 1 mM DTT) and mixed 1:1 with well solution containing 1.4-1.6 M sodium malonate pH 6.5-7.0. Large crystals grown over the course of two weeks were cryoprotected in 2.5 M (total) sodium malonate and flash-frozen in liquid nitrogen. Diffraction data were collected at the Advanced Light source beamline 8.3.1 (support statement below). Data were indexed and reduced with XDS [87], scaled with AIMLESS [88], and converted to structure factors with TRUNCATE [89] (**Table S1**). The structure was determined by molecular replacement in PHASER using the structure of HIM-3 (PDB ID 4TRK) [19] as a search model. An initial model was rebuilt in COOT [90] and refined in phenix.refine [91] using positional and individual B-factor (anisotropic for protein atoms, isotropic for water molecules) refinement with riding hydrogens. Structure figures were generated in PyMOL version 2.0 (Schrödinger, LLC).

ALS Beamline 8.3.1 support statement

The Berkeley Center for Structural Biology is supported in part by the Howard Hughes Medical Institute. The Advanced Light Source is a Department of Energy Office of Science User Facility under Contract No. DE-AC02-05CH11231. The Pilatus detector on 5.0.1. was funded under NIH grant S10OD021832. The ALS-ENABLE beamlines are supported in part by the National Institutes of Health, National Institute of General Medical Sciences, grant P30 GM124169.

Author contributions:

A.E.R., S.G., A.D., K.D.C., and N.B. designed the experiments. A.E.R., S.G., A.D., M.M., V.O., and K.E. performed the experiments. A.E.R., S.G., A.D., M.M., V.O., K.E., K.D.C., and N.B. analyzed the data. A.E.R and N.B. wrote the initial draft of the manuscript and A.E.R., S.G., A.D., M.M., V.O., K.E., K.D.C., and N.B. revised the manuscript. K.D.C., and N.B. acquired funding.

Acknowledgements:

We would like to thank Abby Dernburg, Monique Zetka and Anne Villeneuve for valuable strains and reagents. We would also like to thank the members of the Bhalla lab as well as Brandt Warecki and Alice Devigne for careful review of the manuscript. This work was supported by the NIH (grant number R35GM141835 [N.B.], T32GM008646 [A.E.R] and R35GM144121 [K.D.C.]). Some strains were provided by the CGC, which is funded by NIH Office of Research Infrastructure Programs (P40 OD010440).

References:

1. Hassold T, Hunt P. To err (meiotically) is human: the genesis of human aneuploidy. Nat Rev Genet. 2001;2(4):280-91. doi: 10.1038/35066065. PubMed PMID: 11283700.

2. Deshong AJ, Ye AL, Lamelza P, Bhalla N. A quality control mechanism coordinates meiotic prophase events to promote crossover assurance. PLoS Genet. 2014;10(4):e1004291. doi: 10.1371/journal.pgen.1004291. PubMed PMID: 24762417; PubMed Central PMCID: PMCPMC3998905.

3. Giacopazzi S, Vong D, Devigne A, Bhalla N. PCH-2 collaborates with CMT-1 to proofread meiotic homolog interactions. PLoS Genet. 2020;16(7):e1008904. doi: 10.1371/journal.pgen.1008904. PubMed PMID: 32730253; PubMed Central PMCID: PMCPMC7433886.

4. Aravind L, Koonin EV. The HORMA domain: a common structural denominator in mitotic checkpoints, chromosome synapsis and DNA repair. Trends Biochem Sci. 1998;23(8):284-6. PubMed PMID: 9757827.

5. Ur SN, Corbett KD. Architecture and Dynamics of Meiotic Chromosomes. Annu Rev Genet. 2021;55:497-526. Epub 20210916. doi: 10.1146/annurev-genet-071719-020235. PubMed PMID: 34530636.

6. Hollingsworth NM, Goetsch L, Byers B. The HOP1 gene encodes a meiosis-specific component of yeast chromosomes. Cell. 1990;61(1):73-84. PubMed PMID: 2107981.

7. Lorenz A, Wells JL, Pryce DW, Novatchkova M, Eisenhaber F, McFarlane RJ, et al. S. pombe meiotic linear elements contain proteins related to synaptonemal complex components. J Cell Sci. 2004;117(Pt 15):3343-51. doi: 10.1242/jcs.01203. PubMed PMID: 15226405.

8. Fukuda T, Daniel K, Wojtasz L, Toth A, Hoog C. A novel mammalian HORMA domain-containing protein, HORMAD1, preferentially associates with unsynapsed meiotic chromosomes. Exp Cell Res. 2010;316(2):158-71. doi: 10.1016/j.yexcr.2009.08.007. PubMed PMID: 19686734.

9. Caryl AP, Armstrong SJ, Jones GH, Franklin FC. A homologue of the yeast HOP1 gene is inactivated in the Arabidopsis meiotic mutant asy1. Chromosoma. 2000;109(1-2):62-71. doi: 10.1007/s004120050413. PubMed PMID: 10855496.

10. Wojtasz L, Daniel K, Roig I, Bolcun-Filas E, Xu H, Boonsanay V, et al. Mouse HORMAD1 and HORMAD2, two conserved meiotic chromosomal proteins, are depleted from synapsed chromosome axes with the help of TRIP13 AAA-ATPase. PLoS Genet. 2009;5(10):e1000702. doi: 10.1371/journal.pgen.1000702. PubMed PMID: 19851446; PubMed Central PMCID: PMCPMC2758600.

11. Martinez-Perez E, Villeneuve AM. HTP-1-dependent constraints coordinate homolog pairing and synapsis and promote chiasma formation during C. elegans meiosis. Genes Dev. 2005;19(22):2727-43. doi: 10.1101/gad.1338505. PubMed PMID: 16291646; PubMed Central PMCID: PMCPMC1283965.

12. Goodyer W, Kaitna S, Couteau F, Ward JD, Boulton SJ, Zetka M. HTP-3 links DSB formation with homolog pairing and crossing over during C. elegans meiosis. Dev Cell. 2008;14(2):263-74. doi: 10.1016/j.devcel.2007.11.016. PubMed PMID: 18267094.

13. Couteau F, Zetka M. HTP-1 coordinates synaptonemal complex assembly with homolog alignment during meiosis in C. elegans. Genes Dev. 2005;19(22):2744-56. doi: 10.1101/gad.1348205. PubMed PMID: 16291647; PubMed Central PMCID: PMCPMC1283966.

14. Zetka MC, Kawasaki I, Strome S, Muller F. Synapsis and chiasma formation in Caenorhabditis elegans require HIM-3, a meiotic chromosome core component that functions in chromosome segregation. Genes Dev. 1999;13(17):2258-70. PubMed PMID: 10485848; PubMed Central PMCID: PMC317003.

15. Daniel K, Lange J, Hached K, Fu J, Anastassiadis K, Roig I, et al. Meiotic homologue alignment and its quality surveillance are controlled by mouse HORMAD1. Nat Cell Biol. 2011;13(5):599-610. doi: 10.1038/ncb2213. PubMed PMID: 21478856; PubMed Central PMCID: PMCPMC3087846.

16. Kogo H, Tsutsumi M, Ohye T, Inagaki H, Abe T, Kurahashi H. HORMAD1-dependent checkpoint/surveillance mechanism eliminates asynaptic oocytes. Genes Cells. 2012;17(6):439-54. doi: 10.1111/j.1365-2443.2012.01600.x. PubMed PMID: 22530760.

17. Shin YH, Choi Y, Erdin SU, Yatsenko SA, Kloc M, Yang F, et al. Hormad1 mutation disrupts synaptonemal complex formation, recombination, and chromosome segregation in mammalian meiosis. PLoS Genet. 2010;6(11):e1001190. doi: 10.1371/journal.pgen.1001190. PubMed PMID: 21079677; PubMed Central PMCID: PMCPMC2973818.

18. Wojtasz L, Cloutier JM, Baumann M, Daniel K, Varga J, Fu J, et al. Meiotic DNA double-strand breaks and chromosome asynapsis in mice are monitored by distinct HORMAD2-independent and -dependent mechanisms. Genes Dev. 2012;26(9):958-73. doi: 10.1101/gad.187559.112. PubMed PMID: 22549958; PubMed Central PMCID: PMCPMC3347793.

19. Kim Y, Rosenberg SC, Kugel CL, Kostow N, Rog O, Davydov V, et al. The chromosome axis controls meiotic events through a hierarchical assembly of HORMA domain proteins. Dev Cell. 2014;31(4):487-502. doi: 10.1016/j.devcel.2014.09.013. PubMed PMID: 25446517; PubMed Central PMCID: PMCPMC4254552.

20. Severson AF, Ling L, van Zuylen V, Meyer BJ. The axial element protein HTP-3 promotes cohesin loading and meiotic axis assembly in C. elegans to implement the meiotic program of chromosome segregation. Genes Dev. 2009;23(15):1763-78. doi: 10.1101/gad.1808809. PubMed PMID: 19574299; PubMed Central PMCID: PMCPMC2720254.

21. Couteau F, Nabeshima K, Villeneuve A, Zetka M. A component of C. elegans meiotic chromosome axes at the interface of homolog alignment, synapsis, nuclear reorganization, and recombination. Curr Biol. 2004;14(7):585-92. doi: 10.1016/j.cub.2004.03.033. PubMed PMID: 15062099.

22. Martinez-Perez E, Schvarzstein M, Barroso C, Lightfoot J, Dernburg AF, Villeneuve AM. Crossovers trigger a remodeling of meiotic chromosome axis composition that is linked to two-step loss of sister chromatid cohesion. Genes Dev. 2008;22(20):2886-901. doi: 10.1101/gad.1694108. PubMed PMID: 18923085; PubMed Central PMCID: PMCPMC2569886.

23. Rosenberg SC, Corbett KD. The multifaceted roles of the HORMA domain in cellular signaling. J Cell Biol. 2015;211(4):745-55. doi: 10.1083/jcb.201509076. PubMed PMID: 26598612; PubMed Central PMCID: PMCPMC4657174.

24. Ye Q, Rosenberg SC, Moeller A, Speir JA, Su TY, Corbett KD. TRIP13 is a protein-remodeling AAA+ ATPase that catalyzes MAD2 conformation switching. eLife. 2015;4. Epub 2015/04/29. doi: 10.7554/eLife.07367. PubMed PMID: 25918846; PubMed Central PMCID: PMC4439613.

25. Clairmont CS, Sarangi P, Ponnienselvan K, Galli LD, Csete I, Moreau L, et al. TRIP13 regulates DNA repair pathway choice through REV7 conformational change. Nat Cell Biol. 2020;22(1):87-96. doi: 10.1038/s41556-019-0442-y. PubMed PMID: 31915374; PubMed Central PMCID: PMCPMC7336368.

26. Alfieri C, Chang L, Barford D. Mechanism for remodelling of the cell cycle checkpoint protein MAD2 by the ATPase TRIP13. Nature. 2018;559(7713):274-8. doi: 10.1038/s41586-018-0281-1. PubMed PMID: 29973720; PubMed Central PMCID: PMCPMC6057611.

27. Ye Q, Kim DH, Dereli I, Rosenberg SC, Hagemann G, Herzog F, et al. The AAA+ ATPase TRIP13 remodels HORMA domains through N-terminal engagement and unfolding. EMBO J. 2017. doi: 10.15252/embj.201797291. PubMed PMID: 28659378.

28. West AMV, Komives EA, Corbett KD. Conformational dynamics of the Hop1 HORMA domain reveal a common mechanism with the spindle checkpoint protein Mad2. Nucleic Acids Res. 2017. doi: 10.1093/nar/gkx1196. PubMed PMID: 29186573.

29. Herruzo E, Lago-Maciel A, Baztan S, Santos B, Carballo JA, San-Segundo PA. Pch2 orchestrates the meiotic recombination checkpoint from the cytoplasm. PLoS Genet. 2021;17(7):e1009560. doi: 10.1371/journal.pgen.1009560. PubMed PMID: 34260586; PubMed Central PMCID: PMCPMC8312941.

30. Yang C, Hu B, Portheine SM, Chuenban P, Schnittger A. State changes of the HORMA protein ASY1 are mediated by an interplay between its closure motif and PCH2. Nucleic Acids Res. 2020;48(20):11521-35. doi: 10.1093/nar/gkaa527. PubMed PMID: 32558910; PubMed Central PMCID: PMCPMC7672429.

31. Chen C, Jomaa A, Ortega J, Alani EE. Pch2 is a hexameric ring ATPase that remodels the chromosome axis protein Hop1. Proc Natl Acad Sci U S A. 2014;111(1):E44-53. doi: 10.1073/pnas.1310755111. PubMed PMID: 24367111; PubMed Central PMCID: PMCPMC3890899.

32. Raina VB, Vader G. Homeostatic Control of Meiotic Prophase Checkpoint Function by Pch2 and Hop1. Curr Biol. 2020;30(22):4413-24.e5. Epub 20200910. doi: 10.1016/j.cub.2020.08.064. PubMed PMID: 32916108.

33. Borner GV, Barot A, Kleckner N. Yeast Pch2 promotes domainal axis organization, timely recombination progression, and arrest of defective recombinosomes during meiosis. Proc

Natl Acad Sci U S A. 2008;105(9):3327-32. doi: 10.1073/pnas.0711864105. PubMed PMID: 18305165; PubMed Central PMCID: PMCPMC2265181.

34. Joshi N, Barot A, Jamison C, Borner GV. Pch2 links chromosome axis remodeling at future crossover sites and crossover distribution during yeast meiosis. PLoS Genet. 2009;5(7):e1000557. doi: 10.1371/journal.pgen.1000557. PubMed PMID: 19629172; PubMed Central PMCID: PMCPMC2708914.

35. Lambing C, Osman K, Nuntasoontorn K, West A, Higgins JD, Copenhaver GP, et al. Arabidopsis PCH2 Mediates Meiotic Chromosome Remodeling and Maturation of Crossovers. PLoS Genet. 2015;11(7):e1005372. doi: 10.1371/journal.pgen.1005372. PubMed PMID: 26182244; PubMed Central PMCID: PMCPMC4504720.

36. MacQueen AJ, Phillips CM, Bhalla N, Weiser P, Villeneuve AM, Dernburg AF. Chromosome sites play dual roles to establish homologous synapsis during meiosis in C. elegans. Cell. 2005;123(6):1037-50. doi: 10.1016/j.cell.2005.09.034. PubMed PMID: 16360034; PubMed Central PMCID: PMCPMC4435800.

37. Cuacos M, Lambing C, Pachon-Penalba M, Osman K, Armstrong SJ, Henderson IR, et al. Meiotic chromosome axis remodelling is critical for meiotic recombination in Brassica rapa. J Exp Bot. 2021;72(8):3012-27. doi: 10.1093/jxb/erab035. PubMed PMID: 33502451; PubMed Central PMCID: PMCPMC8023211.

38. San-Segundo PA, Roeder GS. Pch2 links chromatin silencing to meiotic checkpoint control. Cell. 1999;97(3):313-24. PubMed PMID: 10319812.

39. Herruzo E, Ontoso D, Gonzalez-Arranz S, Cavero S, Lechuga A, San-Segundo PA. The Pch2 AAA+ ATPase promotes phosphorylation of the Hop1 meiotic checkpoint adaptor in response to synaptonemal complex defects. Nucleic Acids Res. 2016;44(16):7722-41. doi: 10.1093/nar/gkw506. PubMed PMID: 27257060; PubMed Central PMCID: PMCPMC5027488.

40. MacQueen AJ, Colaiacovo MP, McDonald K, Villeneuve AM. Synapsis-dependent and -independent mechanisms stabilize homolog pairing during meiotic prophase in C. elegans. Genes Dev. 2002;16(18):2428-42. PubMed PMID: 12231631.

41. Carlton PM. Three-dimensional structured illumination microscopy and its application to chromosome structure. Chromosome Res. 2008;16(3):351-65. doi: 10.1007/s10577-008-1231-9. PubMed PMID: 18461477.

42. Couteau F, Zetka M. DNA damage during meiosis induces chromatin remodeling and synaptonemal complex disassembly. Dev Cell. 2011;20(3):353-63. doi: 10.1016/j.devcel.2011.01.015. PubMed PMID: 21397846.

43. Bohr T, Nelson CR, Giacopazzi S, Lamelza P, Bhalla N. Shugoshin Is Essential for Meiotic Prophase Checkpoints in C. elegans. Curr Biol. 2018;28(20):3199-211.e3. Epub 20181004. doi: 10.1016/j.cub.2018.08.026. PubMed PMID: 30293721; PubMed Central PMCID: PMCPMC6200582.

44. Phillips CM, Wong C, Bhalla N, Carlton PM, Weiser P, Meneely PM, et al. HIM-8 binds to the X chromosome pairing center and mediates chromosome-specific meiotic synapsis. Cell. 2005;123(6):1051-63. doi: 10.1016/j.cell.2005.09.035. PubMed PMID: 16360035; PubMed Central PMCID: PMCPMC4435792.

45. Villeneuve AM. A cis-acting locus that promotes crossing over between X chromosomes in Caenorhabditis elegans. Genetics. 1994;136(3):887-902. PubMed PMID: 8005443; PubMed Central PMCID: PMCPMC1205894.

46. Colaiacovo MP, MacQueen AJ, Martinez-Perez E, McDonald K, Adamo A, La Volpe A, et al. Synaptonemal complex assembly in C. elegans is dispensable for loading strand-exchange proteins but critical for proper completion of recombination. Dev Cell. 2003;5(3):463-74. PubMed PMID: 12967565.

47. Yokoo R, Zawadzki KA, Nabeshima K, Drake M, Arur S, Villeneuve AM. COSA-1 reveals robust homeostasis and separable licensing and reinforcement steps governing meiotic crossovers. Cell. 2012;149(1):75-87. doi: 10.1016/j.cell.2012.01.052. PubMed PMID: 22464324; PubMed Central PMCID: PMCPMC3339199.

48. Bhalla N, Dernburg AF. A conserved checkpoint monitors meiotic chromosome synapsis in Caenorhabditis elegans. Science. 2005;310(5754):1683-6. doi: 10.1126/science.1117468. PubMed PMID: 16339446.

49. Stamper EL, Rodenbusch SE, Rosu S, Ahringer J, Villeneuve AM, Dernburg AF. Identification of DSB-1, a protein required for initiation of meiotic recombination in Caenorhabditis elegans, illuminates a crossover assurance checkpoint. PLoS Genet. 2013;9(8):e1003679. doi: 10.1371/journal.pgen.1003679. PubMed PMID: 23990794; PubMed Central PMCID: PMCPMC3749324.

50. Kim Y, Kostow N, Dernburg AF. The Chromosome Axis Mediates Feedback Control of CHK-2 to Ensure Crossover Formation in C. elegans. Dev Cell. 2015;35(2):247-61. doi:

10.1016/j.devcel.2015.09.021. PubMed PMID: 26506311; PubMed Central PMCID: PMCPMC4624198.

51. Rosu S, Zawadzki KA, Stamper EL, Libuda DE, Reese AL, Dernburg AF, et al. The C. elegans DSB-2 protein reveals a regulatory network that controls competence for meiotic DSB formation and promotes crossover assurance. PLoS Genet. 2013;9(8):e1003674. doi: 10.1371/journal.pgen.1003674. PubMed PMID: 23950729; PubMed Central PMCID: PMCPMC3738457.

52. Sievers F, Wilm A, Dineen D, Gibson TJ, Karplus K, Li W, et al. Fast, scalable generation of high-quality protein multiple sequence alignments using Clustal Omega. Mol Syst Biol. 2011;7:539. Epub 20111011. doi: 10.1038/msb.2011.75. PubMed PMID: 21988835; PubMed Central PMCID: PMCPMC3261699.

53. Silva N, Ferrandiz N, Barroso C, Tognetti S, Lightfoot J, Telecan O, et al. The fidelity of synaptonemal complex assembly is regulated by a signaling mechanism that controls early meiotic progression. Dev Cell. 2014;31(4):503-11. doi: 10.1016/j.devcel.2014.10.001. PubMed PMID: 25455309.

54. Martini E, Diaz RL, Hunter N, Keeney S. Crossover homeostasis in yeast meiosis. Cell. 2006;126(2):285-95. doi: 10.1016/j.cell.2006.05.044. PubMed PMID: 16873061; PubMed Central PMCID: PMCPMC1949389.

55. Bohr T, Ashley G, Eggleston E, Firestone K, Bhalla N. Synaptonemal Complex Components Are Required for Meiotic Checkpoint Function in Caenorhabditis elegans.

Genetics. 2016;204(3):987-97. doi: 10.1534/genetics.116.191494. PubMed PMID: 27605049; PubMed Central PMCID: PMCPMC5105873.

56. West AMV, Komives EA, Corbett KD. Conformational dynamics of the Hop1 HORMA domain reveal a common mechanism with the spindle checkpoint protein Mad2. Nucleic Acids Res. 2018;46(1):279-92. doi: 10.1093/nar/gkx1196. PubMed PMID: 29186573; PubMed Central PMCID: PMCPMC5758881.

57. Ma HT, Poon RY. TRIP13 Regulates Both the Activation and Inactivation of the Spindle-Assembly Checkpoint. Cell Rep. 2016;14(5):1086-99. doi: 10.1016/j.celrep.2016.01.001. PubMed PMID: 26832417.

58. Ma HT, Poon RYC. TRIP13 Functions in the Establishment of the Spindle Assembly Checkpoint by Replenishing O-MAD2. Cell Rep. 2018;22(6):1439-50. doi: 10.1016/j.celrep.2018.01.027. PubMed PMID: 29425500.

59. Nelson CR, Hwang T, Chen PH, Bhalla N. TRIP13PCH-2 promotes Mad2 localization to unattached kinetochores in the spindle checkpoint response. J Cell Biol. 2015;211(3):503-16. doi: 10.1083/jcb.201505114. PubMed PMID: 26527744; PubMed Central PMCID: PMCPMC4639874.

60. Eytan E, Wang K, Miniowitz-Shemtov S, Sitry-Shevah D, Kaisari S, Yen TJ, et al. Disassembly of mitotic checkpoint complexes by the joint action of the AAA-ATPase TRIP13 and p31(comet). Proc Natl Acad Sci U S A. 2014;111(33):12019-24. doi: 10.1073/pnas.1412901111. PubMed PMID: 25092294; PubMed Central PMCID: PMCPMC4142996.

61. Wang K, Sturt-Gillespie B, Hittle JC, Macdonald D, Chan GK, Yen TJ, et al. Thyroid hormone receptor interacting protein 13 (TRIP13) AAA-ATPase is a novel mitotic checkpoint-silencing protein. J Biol Chem. 2014;289(34):23928-37. doi: 10.1074/jbc.M114.585315. PubMed PMID: 25012665; PubMed Central PMCID: PMCPMC4156041.

62. Defachelles L, Russo AE, Nelson CR, Bhalla N. The conserved AAA-ATPase PCH-2 (TRIP13) regulates spindle checkpoint strength. Mol Biol Cell. 2020;31(20):2219-33. doi: 10.1091/mbc.E20-05-0310. PubMed PMID: 32697629; PubMed Central PMCID: PMCPMC7550697.

63. Sanchez-Moran E, Santos JL, Jones GH, Franklin FC. ASY1 mediates AtDMC1-dependent interhomolog recombination during meiosis in Arabidopsis. Genes Dev. 2007;21(17):2220-33. doi: 10.1101/gad.439007. PubMed PMID: 17785529; PubMed Central PMCID: PMCPMC1950860.

64. Raina VB, Vader G. Homeostatic Control of Meiotic Prophase Checkpoint Function by Pch2 and Hop1. Curr Biol. 2020. doi: 10.1016/j.cub.2020.08.064. PubMed PMID: 32916108.

65. Subramanian VV, MacQueen AJ, Vader G, Shinohara M, Sanchez A, Borde V, et al. Chromosome Synapsis Alleviates Mek1-Dependent Suppression of Meiotic DNA Repair. PLoS Biol. 2016;14(2):e1002369. doi: 10.1371/journal.pbio.1002369. PubMed PMID: 26870961; PubMed Central PMCID: PMCPMC4752329.

66. Dernburg AF, McDonald K, Moulder G, Barstead R, Dresser M, Villeneuve AM. Meiotic recombination in C. elegans initiates by a conserved mechanism and is dispensable for homologous chromosome synapsis. Cell. 1998;94(3):387-98. PubMed PMID: 9708740.

67. Capilla-Perez L, Durand S, Hurel A, Lian Q, Chambon A, Taochy C, et al. The synaptonemal complex imposes crossover interference and heterochiasmy in Arabidopsis. Proc Natl Acad Sci U S A. 2021;118(12). doi: 10.1073/pnas.2023613118. PubMed PMID: 33723072; PubMed Central PMCID: PMCPMC8000504.

68. Cole F, Kauppi L, Lange J, Roig I, Wang R, Keeney S, et al. Homeostatic control of recombination is implemented progressively in mouse meiosis. Nat Cell Biol. 2012;14(4):424-30. doi: 10.1038/ncb2451. PubMed PMID: 22388890; PubMed Central PMCID: PMCPMC3319518.

69. Joshi N, Brown MS, Bishop DK, Borner GV. Gradual implementation of the meiotic recombination program via checkpoint pathways controlled by global DSB levels. Mol Cell. 2015;57(5):797-811. doi: 10.1016/j.molcel.2014.12.027. PubMed PMID: 25661491; PubMed Central PMCID: PMCPMC4392720.

70. Morgan C, Fozard JA, Hartley M, Henderson IR, Bomblies K, Howard M. Diffusion-mediated HEI10 coarsening can explain meiotic crossover positioning in Arabidopsis. Nat Commun. 2021;12(1):4674. doi: 10.1038/s41467-021-24827-w. PubMed PMID: 34344879; PubMed Central PMCID: PMCPMC8333306.

71. Bhalla N. PCH-2 and meiotic HORMADs: A module for evolutionary innovation in meiosis? Current Topics in Developmental Biology. 2022;in press. doi: https://doi.org/10.1016/bs.ctdb.2022.07.001.

72. Das D, Chen SY, Arur S. ERK phosphorylates chromosomal axis component HORMA domain protein HTP-1 to regulate oocyte numbers. Sci Adv. 2020;6(44). Epub 20201030. doi:

10.1126/sciadv.abc5580. PubMed PMID: 33127680; PubMed Central PMCID: PMCPMC7608811.

73. Shin YH, McGuire MM, Rajkovic A. Mouse HORMAD1 is a meiosis i checkpoint protein that modulates DNA double- strand break repair during female meiosis. Biol Reprod. 2013;89(2):29. doi: 10.1095/biolreprod.112.106773. PubMed PMID: 23759310; PubMed Central PMCID: PMCPMC4076362.

74. Kogo H, Tsutsumi M, Inagaki H, Ohye T, Kiyonari H, Kurahashi H. HORMAD2 is essential for synapsis surveillance during meiotic prophase via the recruitment of ATR activity. Genes Cells. 2012;17(11):897-912. doi: 10.1111/gtc.12005. PubMed PMID: 23039116.

75. Baudat F, Manova K, Yuen JP, Jasin M, Keeney S. Chromosome synapsis defects and sexually dimorphic meiotic progression in mice lacking Spo11. Mol Cell. 2000;6(5):989-98. PubMed PMID: 11106739.

76. Giroux CN, Dresser ME, Tiano HF. Genetic control of chromosome synapsis in yeast meiosis. Genome. 1989;31(1):88-94. PubMed PMID: 2687110.

77. Grelon M, Vezon D, Gendrot G, Pelletier G. AtSPO11-1 is necessary for efficient meiotic recombination in plants. EMBO J. 2001;20(3):589-600. doi: 10.1093/emboj/20.3.589. PubMed PMID: 11157765; PubMed Central PMCID: PMCPMC133473.

78. Romanienko PJ, Camerini-Otero RD. The mouse Spo11 gene is required for meiotic chromosome synapsis. Mol Cell. 2000;6(5):975-87. PubMed PMID: 11106738.

79. Heldrich J, Milano CR, Markowitz TE, Ur SN, Vale-Silva LA, Corbett KD, et al. Two pathways drive meiotic chromosome axis assembly in Saccharomyces cerevisiae. Nucleic Acids Res. 2022;50(8):4545-56. doi: 10.1093/nar/gkac227. PubMed PMID: 35412621; PubMed Central PMCID: PMCPMC9071447.

80. Subramanian VV, Zhu X, Markowitz TE, Vale-Silva LA, San-Segundo PA, Hollingsworth NM, et al. Persistent DNA-break potential near telomeres increases initiation of meiotic recombination on short chromosomes. Nat Commun. 2019;10(1):970. doi: 10.1038/s41467-019-08875-x. PubMed PMID: 30814509; PubMed Central PMCID: PMCPMC6393486.

81. Brenner S. The genetics of Caenorhabditis elegans. Genetics. 1974;77(1):71-94. PubMed PMID: 4366476; PubMed Central PMCID: PMCPMC1213120.

82. Arribere JA, Bell RT, Fu BX, Artiles KL, Hartman PS, Fire AZ. Efficient marker-free recovery of custom genetic modifications with CRISPR/Cas9 in Caenorhabditis elegans. Genetics. 2014;198(3):837-46. doi: 10.1534/genetics.114.169730. PubMed PMID: 25161212; PubMed Central PMCID: PMCPMC4224173.

83. Wickham H. ggplot2: Elegant Graphics for Data Analysis. New York: Springer-Verlag; 2016.

84. Toraason E, Adler VL, Kurhanewicz NA, DiNardo A, Saunders AM, Cahoon CK, et al. Automated and customizable quantitative image analysis of whole Caenorhabditis elegans germlines. Genetics. 2021;217(3). doi: 10.1093/genetics/iyab010. PubMed PMID: 33772283; PubMed Central PMCID: PMCPMC8045727.

85. Preibisch S, Saalfeld S, Tomancak P. Globally optimal stitching of tiled 3D microscopic image acquisitions. Bioinformatics. 2009;25(11):1463-5. Epub 20090403. doi: 10.1093/bioinformatics/btp184. PubMed PMID: 19346324; PubMed Central PMCID: PMCPMC2682522.

86. Tropea JE, Cherry S, Waugh DS. Expression and purification of soluble His(6)-tagged TEV protease. Methods in Molecular Biology. 498. Totowa, NJ: Humana Press; 2009. p. 297-307.

87. Kabsch W. XDS. Acta crystallographica Section D, Biological crystallography. 2010;66:125-32. doi: 10.1107/S0907444909047337. PubMed PMID: 20124692.

88. Evans PR, Murshudov GN. How good are my data and what is the resolution? Acta crystallographica Section D, Biological crystallography. 2013;69:1204-14. doi: 10.1107/S0907444913000061. PubMed PMID: 23793146.

89. Winn MD, Ballard CC, Cowtan KD, Dodson EJ, Emsley P, Evans PR, et al. Overview of the CCP4 suite and current developments. Acta crystallographica Section D, Biological crystallography. 2011;67:235-42. doi: 10.1107/S0907444910045749. PubMed PMID: 21460441.

90. Emsley P, Lohkamp B, Scott WG, Cowtan K. Features and development of Coot. Acta crystallographica Section D, Biological crystallography. 2010;66:486-501. doi: 10.1107/S0907444910007493. PubMed PMID: 20383002.

91. Adams PD, Afonine PV, Bunkóczi G, Chen VB, Davis IW, Echols N, et al. PHENIX: a comprehensive Python-based system for macromolecular structure solution. Acta

crystallographica Section D, Biological crystallography. 2010;66:213-21. doi: 10.1107/S0907444909052925.

92. Varadi M, Anyango S, Deshpande M, Nair S, Natassia C, Yordanova G, et al. AlphaFold Protein Structure Database: massively expanding the structural coverage of protein-sequence space with high-accuracy models. Nucleic Acids Res. 2022;50(D1):D439-D44. doi: 10.1093/nar/gkab1061. PubMed PMID: 34791371; PubMed Central PMCID: PMCPMC8728224.

Figure Legends

Figure 1. PCH-2's localization is consistent with remodeling HORMADs on meiotic axes. **A.** Cartoon of synaptonemal complex with axial elements made up of meiotic HORMADs and the central element component, SYP-1. **B.** Structured illumination microscopy (SIM) images of meiotic nuclei stained with antibodies against PCH-2 (green) and SYP-1 (magenta). Arrows represent regions of PCH-2 potentially associated with meiotic axes. Scalebar indicates 5 microns. **C.** Cropped insets of PCH-2 and SYP-1 signal. Yellow line represents area of pixel intensities measured. **D**. Line scans of PCH-2 (green) and SYP-1 (magenta) pixel intensities plotted against distance in pixels.

Figure 2. HORMA domain structure of meiotic HORMADs in *C. elegans.* **A.** Cartoon depicting protein domains of HTP-3, HIM-3, HTP-1, and HTP-2. HORMA domains and closure motifs are shown as colored boxes and labeled. Mutations generated by CRISPR/Cas9 are shown. **B.** Clustal Omega alignment of the HORMA domains of HTP-3, HIM-3, HTP-1, and HTP-2. Asterisks represent conserved residues, : represents conservative changes and . represents semi-conservative changes. Red box indicates targeted reside for mutation for each respective HORMAD. **C.** Structure of the *C. elegans* HTP-3 HORMA domain (pink) bound to a closure motif (gray), predicted by AlphaFold 2 [92]. Right panels show the position of H96. **D.** Overlay of wild-type (gray; PDB ID 4TRK) and R93Y mutant (green/pink) of *C. elegans* HIM-3. Right panels show the position of residue 93 and show that the overall HORMA domain structure is not impacted upon mutation of arginine 93 to tyrosine. **E.** View of the *C. elegans* HTP-1 HORMA domain (PDB ID 4TZQ) equivalent to the close-up panel in (D), showing the position of residue G97 (yellow spheres), which is partially buried against a neighboring alpha-helix.

Figure 3. *htp-3^{H96Y}* suppresses the acceleration of pairing and synapsis but exacerbates defects in DNA repair and crossover formation in *pch-2* mutants. A. Cartoon depicting zones for quantification in the *C. elegans* germline. **B.** Meiotic nuclei stained with DAPI (magenta) and antibody against HIM-8 (green). **C.** Quantification of percent nuclei with paired HIM-8 signals in zones 1-6 for *syp-1* (blue), *pch-2;syp-1* (red), *htp-3^{H96Y};syp-1* (green) and *pch-2;htp-3^{H96Y};syp*-1 (purple) mutant strains. Error bars represent 95% confidence intervals. **D.** Meiotic nuclei stained with antibodies against SYP-1(magenta) and HTP-3 (green). Arrows indicates unsynapsed chromosomes. **E.** Quantification of percent nuclei with complete synapsis in zones 1-6 for wildtype (blue), *pch-2* (red), *htp-3^{H96Y}* (green) and *pch-2;htp-3^{H96Y}* (purple) mutant strains. Error bars represent 95% confidence intervals. **F.** Quantification of percent nuclei with complete synapsis in zones 1-6 for *meDf2/*+ (blue), *pch-2;meDf2/*+ (red), *htp-3^{H96Y};meDf2/*+ (green) and *pch-2;htp-3^{H96Y};meDf2/*+ (purple) mutant strains. Error bars represent 95% confidence intervals. **G.** Meiotic nuclei stained with DAPI (magenta) and antibody against RAD-51 (green). **H.** Quantification of average number of RAD-51 foci in zones 1-6 for wildtype (blue), *pch-2* (red), *htp-3^{H96Y}* (green) and *pch-2;htp-3^{H96Y}* (purple) mutant strains. Error bars represent standard error of the mean (SEM). **I.** Meiotic nuclei stained with DNA (magenta) and antibody against GFP::COSA-1 (green). Left indicates representative nuclei with 6 GFP::COSA-1 foci. Right indicates representative nuclei with 5 GFP::COSA-1 foci. **J.** Quantification of percent nuclei with 5 GFP::COSA-1 foci for wildtype, *pch-2*, *htp-3^{H96Y}*, and *pch-2;htp-3^{H96Y}* mutant strains. Error bars represent 95% confidence intervals. In all images, scalebar indicates 5 microns. In all graphs, ** indicates p-value < 0.01 and **** indicated p-value <0.0001, Significance was assessed using two-tailed Fisher's exact-tests.

Figure 4. *him-3^{R93Y}* does not suppress the acceleration of pairing, synapsis, or DNA repair, but does suppress defects in crossover formation in *pch-2* mutants. A. Meiotic nuclei stained with DAPI (magenta) and antibody against HIM-8 (green). **B.** Quantification of

percent nuclei with paired HIM-8 signals in zones 1-6 for *syp-1* (blue), *pch-2;syp-1* (red), *him-3^{R93Y};syp-1* (green) and *pch-2;him-3^{R93Y};syp*-1 (purple) mutant strains. Error bars represent 95% confidence intervals. **C.** Meiotic nuclei stained with antibodies against SYP-1(magenta) and HTP-3 (green). Arrow indicates unsynapsed chromosomes. **D.** Quantification of percent nuclei with complete synapsis in zones 1-6 for wildtype (blue), *pch-2* (red), *him-3^{R93Y}* (green) and *pch-2;him-3^{R93Y}* (purple) mutant strains. Error bars represent 95% confidence intervals. **E.** Quantification of percent nuclei with complete synapsis in zones 1-6 for *meDf2/+* (blue), *pch-2;meDf2/+* (red), *him-3^{R93Y};meDf2/+* (green) and *pch-2;him-3^{R93Y};meDf2/+* (purple) mutant strains. Error bars represent 95% confidence intervals. **F.** Meiotic nuclei stained with DAPI (magenta) and antibody against RAD-51 (green). **G.** Quantification of average number of RAD-51 foci in zones 1-6 for wildtype (blue), *pch-2* (red), *him-3^{R93Y}* (green) and *pch-2;him-3^{R93Y}* (purple) mutant strains. Error bars represent standard error of the mean (SEM). **H.** Meiotic nuclei stained with DNA (magenta) and antibody against GFP::COSA-1 (green). Left indicates representative nuclei with 6 GFP::COSA-1 foci. Right indicates representative nuclei with 5 GFP::COSA-1 foci. **I.** Quantification of percent nuclei with 5 GFP::COSA-1 foci for wildtype, *pch-2*, *him-3^{R93Y}*, and *pch-2;him-3^{R93Y}* mutant strains. Error bars represent 95% confidence intervals. **J.** Oocytes stained with DAPI. Left indicates representative oocyte with zero univalents. Right indicates representative oocyte with univalents (arrows). Scalebar indicates 5 microns. **K.** Quantification of percent oocytes with univalents for wildtype, *pch-2*, *him-3^{R93Y}*, and *pch-2;him-3^{R93Y}* mutant strains. Error bars represent 95% confidence intervals. In all graphs, NS indicates non-significant, * indicates p-value < 0.05, ** indicates p-value < 0.01, *** indicates p-value < 0.001, and **** indicated p-value <0.0001. Significance was assessed using two-tailed Fisher's exact-tests. In all images, scalebar indicates 5 microns.

Figure 5. *htp-1^{G97T}* does not genetically interact with *pch-2* in the context of pairing, synapsis, DNA repair, or crossover formation. A. Meiotic nuclei stained with DAPI (magenta)

and antibody against HIM-8 (green). **B.** Quantification of percent nuclei with paired HIM-8 signals in zones 1-6 for *syp-1* (blue), *pch-2;syp-1* (red), *htp-1^{G97T};syp-1* (green) and *pch-2;htp-1^{G97T};syp*-1 (purple) mutant strains. Error bars represent 95% confidence intervals. **C.** Meiotic nuclei stained with antibodies against SYP-1(magenta) and HTP-3 (green). Arrow indicates unsynapsed chromosomes. **D.** Quantification of percent nuclei with complete synapsis in zones 1-6 for wildtype (blue), *pch-2* (red), *htp-1^{G97T}* (green) and *pch-2;htp-1^{G97T}* (purple) mutant strains. Error bars represent 95% confidence intervals. **E.** Meiotic nuclei stained with DAPI (magenta) and antibody against RAD-51 (green). **F.** Quantification of average number of RAD-51 foci in zones 1-6 for wildtype (blue), *pch-2* (red), *htp-1^{G97T}* (green) and *pch-2;htp-1^{G97T}* (purple) mutant strains. Error bars represent standard error of the mean (SEM). **G.** Meiotic nuclei stained with DNA (magenta) and antibodies against GFP::COSA-1 (green). Left indicates representative nuclei with 6 GFP::COSA-1 foci. Right indicates representative nuclei with 5 GFP::COSA-1 foci. **H.** Quantification of distribution of GFP::COSA-1 foci per nucleus for wildtype (blue), *pch-2* (red), *htp-1^{G97T}* (green) and *pch-2;htp-1^{G97T}* (purple) mutant strains. **E.** Oocytes stained with DAPI. Left indicates representative oocyte with zero univalents. Right indicates representative oocyte with univalents (arrows). **F.** Quantification of percent oocytes with univalents for wildtype, *pch-2*, *htp-1^{G97Y}*, and *pch-2;htp-1^{G97Y}* mutant strains. In all graphs, NS indicates non-significant and **** indicates p-value < 0.0001. Significance was assessed using two-tailed Fisher's exact tests. In all images, scalebar indicates 5 microns.

Figure 6. *htp-1^{G97T}* delays meiotic progression and this delay is partially suppressed by mutation of *pch-2*. A. Full length representative germlines stained with DAPI (magenta) and antibody against DSB-1 (green). Yellow dashed line represents region of DSB-1 positive nuclei. Scalebar indicates 20 microns. **B.** Quantification of DSB-1 positive meiotic nuclei for wildtype, *htp-1^{G97A}, htp-1^{G97S}, htp-1^{G97T} and pch-2;htp-1^{G97T}* mutant strains. NS indicates non-significant. ** indicates p-value <0.01. *** indicates p-value < 0.001. **** indicates p-value <0.0001. Statistical

significance was assessed using two-tailed Fisher's exact tests. Error bars represent 95% confidence intervals.

Figure 7. *him-3^{R93Y}* mutants have reduced affinity for closure motifs. A. Fluorescence polarization peptide binding assay of HIM-3 (blue) and HIM-3^{R93Y} (green) and measured Kd's. **B.** Cartoon depicting proposed model for open and closed conformation switching of wildtype HIM-3 and HIM-3^{R93Y}.

Figure 8. PCH-2 distributes its regulation of meiotic prophase events by remodeling different meiotic HORMADs. Cartoon depicting proposed model for PCH-2's regulation of meiotic prophase events. PCH-2 regulates the progression of pairing and by acting through HTP-3, crossover recombination through HIM-3, and may regulate meiotic progression through HTP-1.

Figure S1. *htp-3^{H96Y}* does not affect meiotic progression. A. Full length representative germlines stained with DAPI (magenta) and DSB-1 (green). Yellow dashed line represents region of DSB-1 positive nuclei. Scalebar indicates 20 microns. **B.** Quantification of DSB-1 positive meiotic nuclei for wildtype and *htp-3 ^{H96Y}* mutant strains. NS indicates non-significant. **C.** Quantification of DSB-1 positive meiotic nuclei for *syp-1* and *htp-3 ^{H96Y};syp-1* mutants. NS indicates non-significant. Statistical significance was assessed using two-tailed Fisher's exact tests. Error bars represent 95% confidence intervals.

Figure S2. *him-3^{R93Y}* localizes to meiotic chromosomes. Top: Mid-pachytene nuclei from wildtype and *him-3^{R93Y}* germlines stained with DAPI (magenta) and antibody against HIM-3 (green). **Bottom:** Mid-pachytene nuclei from wildtype and *him-3^{R93Y}* germlines stained with HIM-3 (white). Scalebar indicates 5 microns.

Figure S3. *him-3^{R93Y}* does not affect meiotic progression. A. Full length representative germlines stained with DAPI (magenta) and antibody against DSB-1 (green). Yellow dashed line represents region of DSB-1 positive nuclei. Scalebar indicates 20 microns. **B.** Quantification of DSB-1 positive meiotic nuclei for wildtype and *him-3^{R93Y}* mutant strains. NS indicates non-significant. **C.** Quantification of DSB-1 positive meiotic nuclei for *syp-1* and *him-3^{R93Y};syp-1* mutants. NS indicates non-significant. Statistical significance was assessed using two-tailed Fisher's exact tests.

Figure S4. *htp-1^{G97T}* localizes to meiotic chromosomes. Top: Mid-pachytene nuclei from wildtype, *htp-1^{G97T}* and *htp-1^{G97T} htp-2* germlines stained with DAPI (magenta) and antibody against HTP-1/2 (green). **Bottom:** Mid-pachytene nuclei from wildtype, *htp-1^{G97T}* and *htp-1^{G97T} htp-2* germlines stained with HTP-1/2 (white). Scalebar indicates 5 microns.

Figure S5. HIM3^{R93Y} does not affect HIM-3's protein stability. Stability curve for purified wildtype HIM-3 (blue) and HIM-3^{R93Y} (green).

Figure S6. *him-3^{R93Y}* and *htp-1^{G97T}* mutants have functional meiotic checkpoints. Quantification of the average number of apoptotic nuclei per germline. NS indicates non-significant and **** indicates p-value <0.0001. Statistical significance was assessed using two-tailed Student t-tests. Error bars indicate 2X standard error of the mean (SEM).

Table 1. Viability assay and male counts for meiotic HORMAD mutants. Table with percent viable progeny and males. Total number of progeny listed in parentheses.

Table S1. Data collection and refinement statistics. Table with data collection and refinement statistics for Figure 7. Explanations of equations listed below the table.

Table 1: Viability and percent male-self-progeny

genotype	percent viability (total no. of animals)	percent male self-progeny
wildtype	100% (2489)	0.22%
meDf2/+	97% (2286)	10.91%
pch-2	100% (2388)	0.71%
pch-2;meDf2/+	98.15% (1808)	0.83%
htp-3^{H96Y}	100% (2586)	0.12%
htp-3^{H96Y}*;meDf2/+*	97.03% (1957)	11.34%
pch-2;htp-3^{H96Y}	81.89% (1067)	1.12%
pch-2;htp-3^{H96Y}*;meDf2/+*	83.90% (1652)	10.84%
him-3^{R93Y}	100% (3304)	0.15%
him-3^{R93Y}*;meDf2/+*	97.69% (3170)	11.30%
pch-2;him-3^{R93Y}	100% (3027)	0.03%
pch-2;him-3^{R93Y}*;meDf2/+*	98.43% (3140)	10.34%
htp-1^{G97T}	67.29% (1984)	2.25%
pch-2;htp-1^{G97T}	58.44% (2175)	1.97%

A

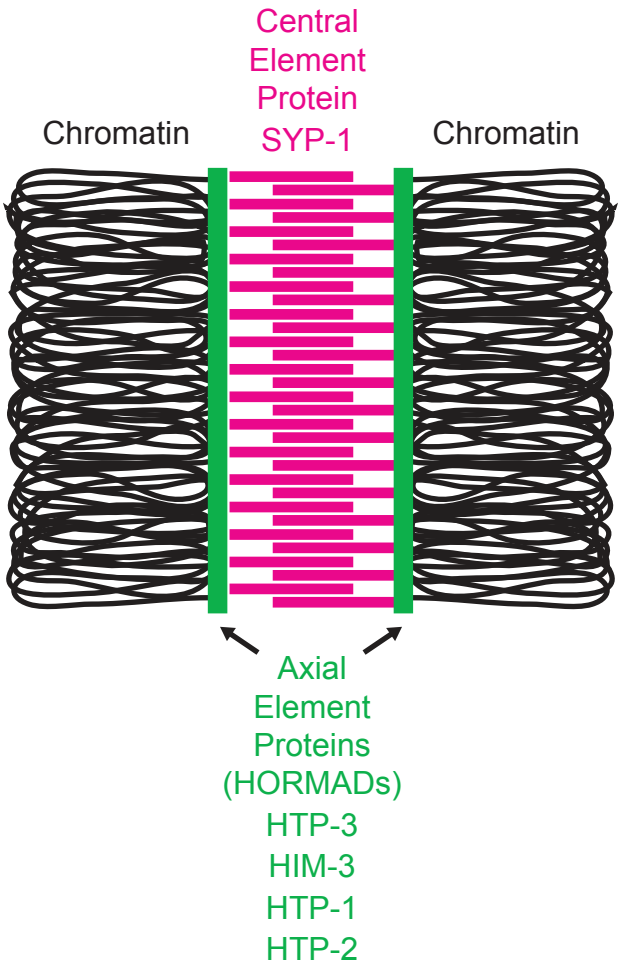
Central
Element
Protein
SYP-1
Chromatin
Chromatin
Axial
Element
Proteins
(HORMADs)
HTP-3
HIM-3
HTP-1
HTP-2

B

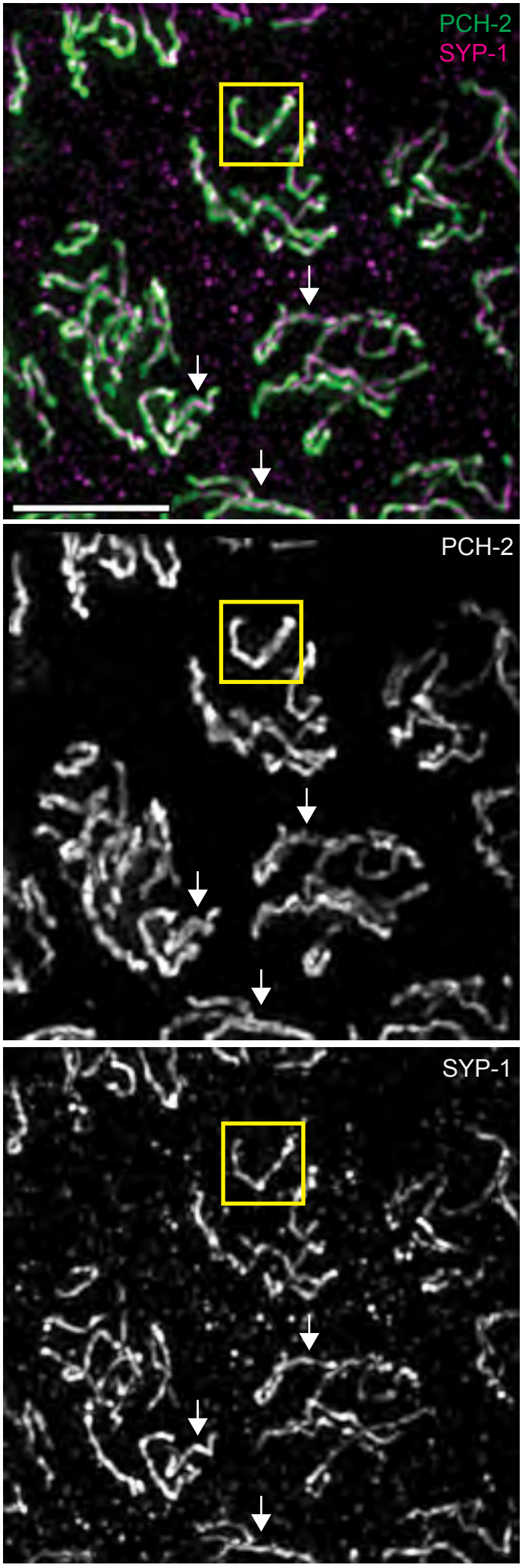
PCH-2
SYP-1
PCH-2
SYP-1

C

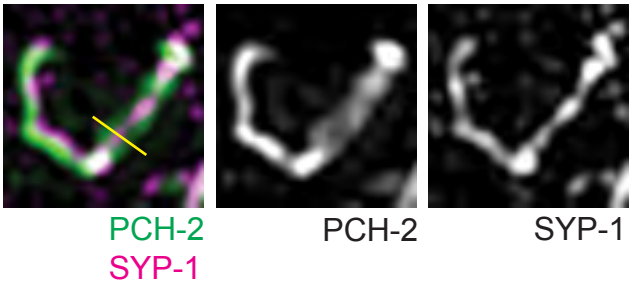
PCH-2
SYP-1
PCH-2
SYP-1

D

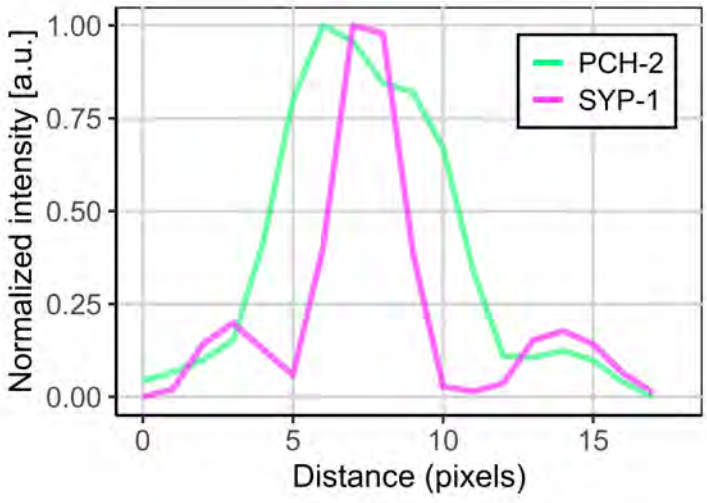
Normalized intensity [a.u.]
1.00
0.75
0.50
0.25
0.00
0
5
10
15
Distance (pixels)
PCH-2
SYP-1

Figure 2

A

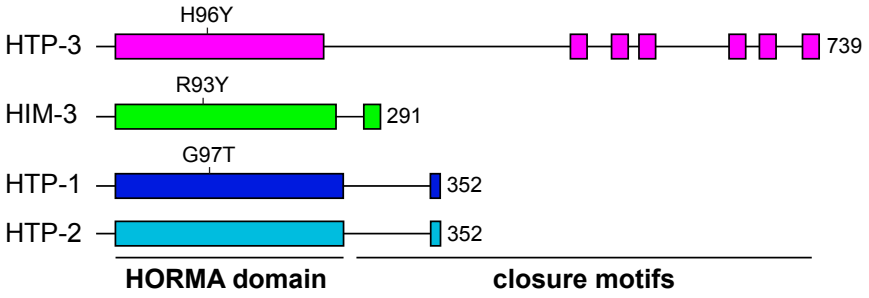

B

```
HTP-3 (57-116) VIPAEYFQDFQVYGDVSGYTLRQDIPEGRSVSSKLLASHDAIRQKLLQKLAIVVEESLN-
HIM-3 (55-114) ILDEKCFKTRTIDKLL-VTAFQSSVPAAKRVSSTFDGLRDAIQQGYLREFAIVFYKKPNE
HTP-1 (59-118) ILGQEYFTKNYITEKLKCMTLCFRNPRSNQIAQLLRNAGDATKDGFLKEVSLVITNNEGD
HTP-2 (59-118) ILEKEYFSKNYITENLSCMTLSFKNLRAHQIAQLLRAAGDATKDGFLKEISLVVTEHDGD
               ::  : *    :   :   ::      .. ::. :    ** ::  *::.::*. :  .
```

C

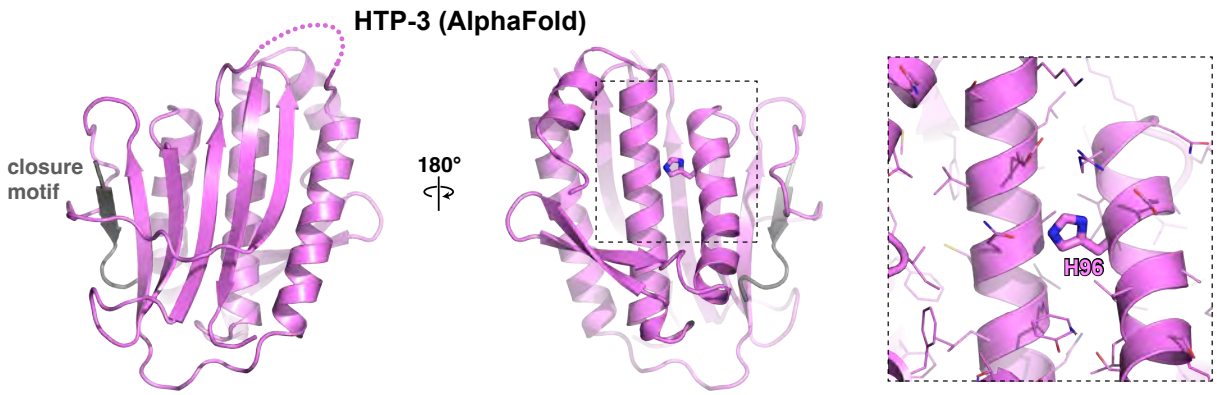

D

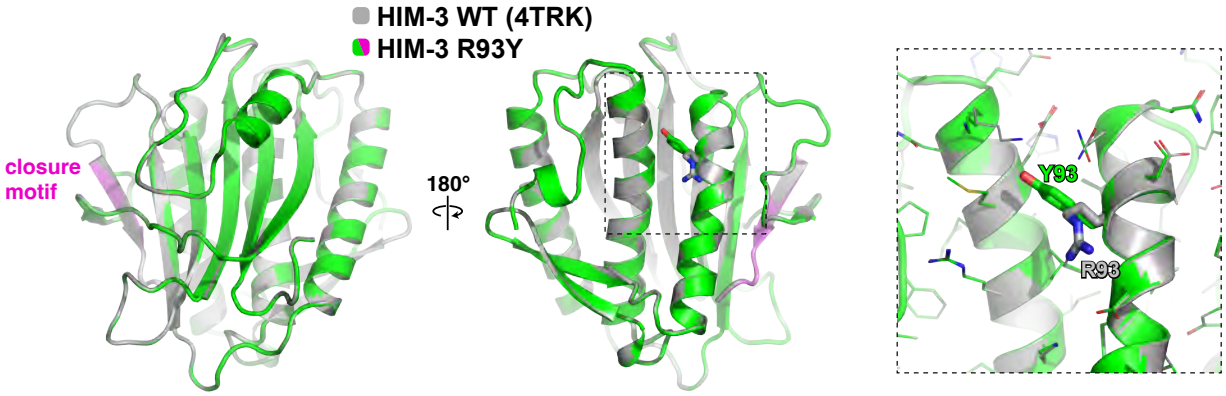

E

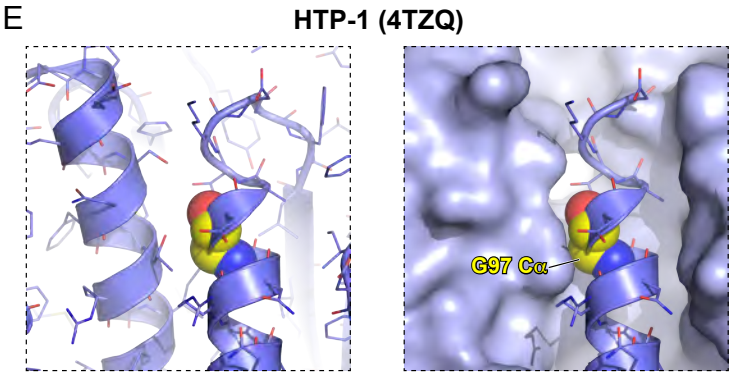

Figure 3

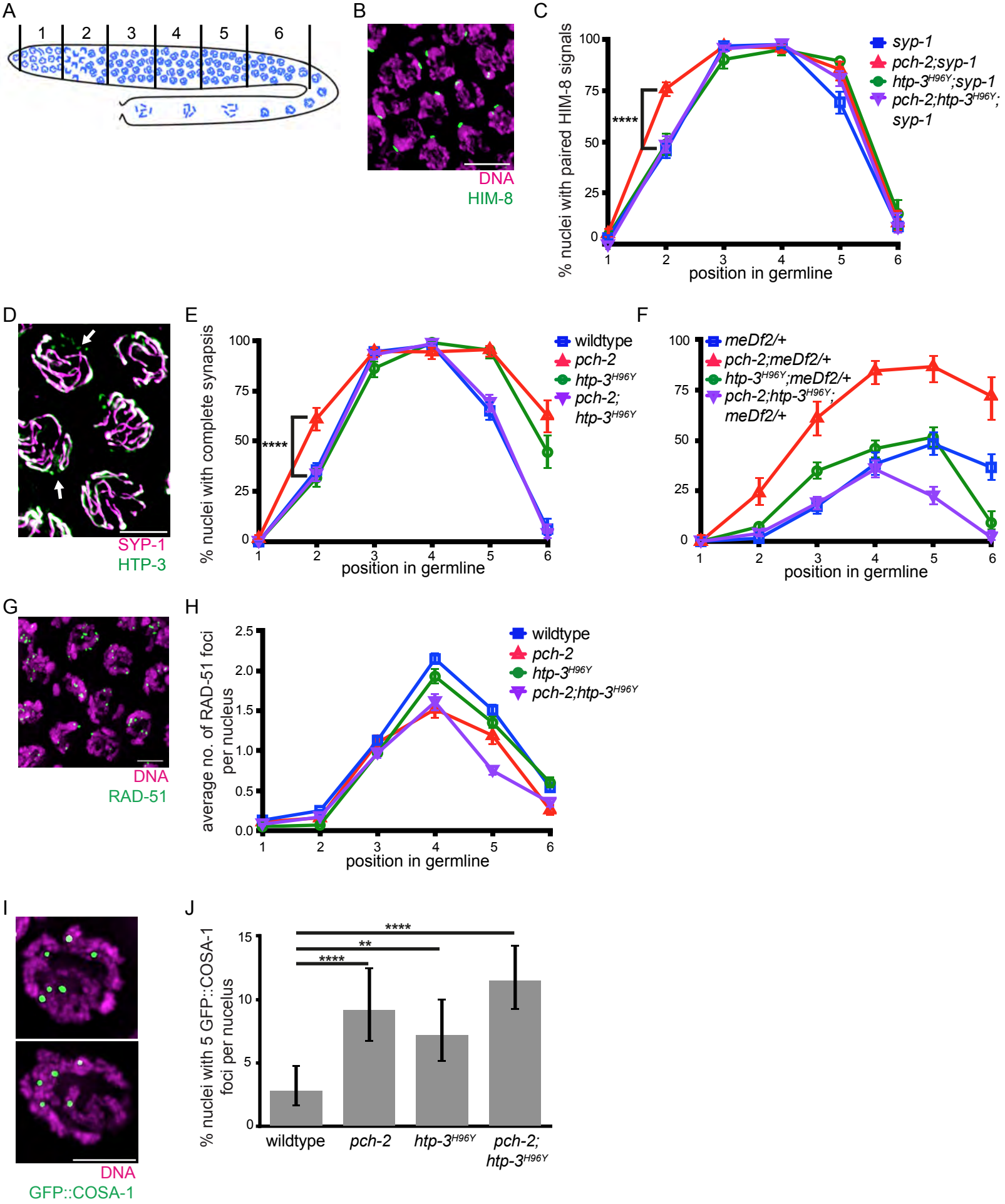
A
1
2
3
4
5
6
B
DNA
HIM-8
C
% nuclei with paired HIM-8 signals
position in germline
syp-1
pch-2;syp-1
htp-3H96Y;syp-1
pch-2;htp-3H96Y;
syp-1
****
D
SYP-1
HTP-3
E
% nuclei with complete synapsis
position in germline
wildtype
pch-2
htp-3H96Y
pch-2;
htp-3H96Y
****
F
meDf2/+
pch-2;meDf2/+
htp-3H96Y;meDf2/+
pch-2;htp-3H96Y;
meDf2/+
position in germline
G
DNA
RAD-51
H
average no. of RAD-51 foci
per nucleus
position in germline
wildtype
pch-2
htp-3H96Y
pch-2;htp-3H96Y
I
DNA
GFP::COSA-1
J
% nuclei with 5 GFP::COSA-1
foci per nucelus
****
**
****
wildtype
pch-2
htp-3H96Y
pch-2;
htp-3H96Y

Figure 4

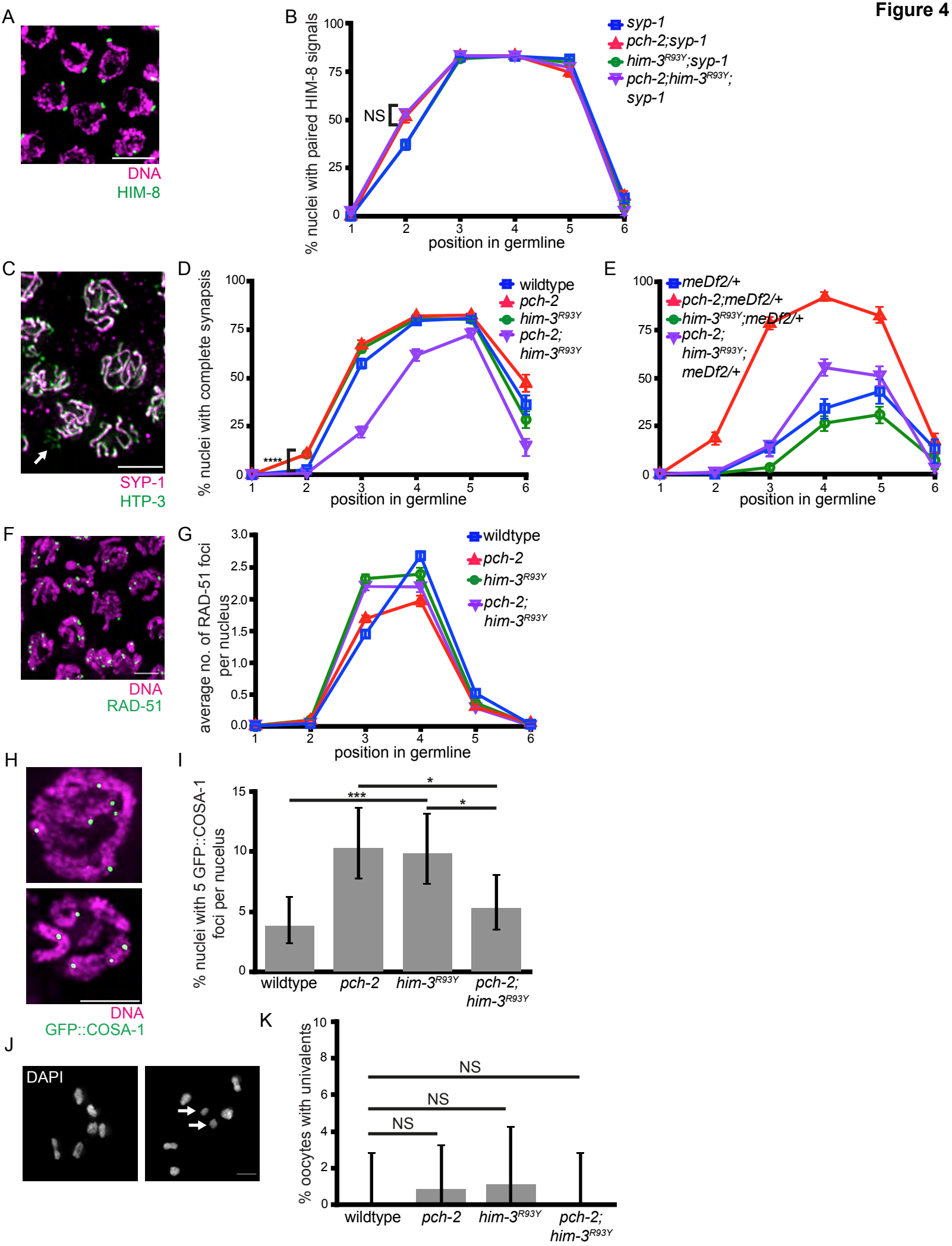
A
DNA
HIM-8
B
% nuclei with paired HIM-8 signals
position in germline
NS
syp-1
pch-2;syp-1
him-3R93Y;syp-1
pch-2;him-3R93Y; syp-1
C
SYP-1
HTP-3
D
% nuclei with complete synapsis
position in germline
****
wildtype
pch-2
him-3R93Y
pch-2; him-3R93Y
E
meDf2/+
pch-2;meDf2/+
him-3R93Y;meDf2/+
pch-2; him-3R93Y; meDf2/+
position in germline
F
DNA
RAD-51
G
average no. of RAD-51 foci per nucleus
position in germline
wildtype
pch-2
him-3R93Y
pch-2; him-3R93Y
H
DNA
GFP::COSA-1
I
% nuclei with 5 GFP::COSA-1 foci per nucelus
***
*
*
wildtype
pch-2
him-3R93Y
pch-2; him-3R93Y
J
DAPI
K
% oocytes with univalents
NS
NS
NS
wildtype
pch-2
him-3R93Y
pch-2; him-3R93Y

Figure 5

A

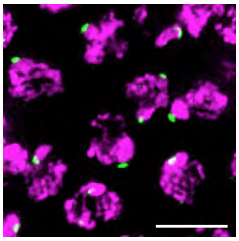

DNA
HIM-8

B

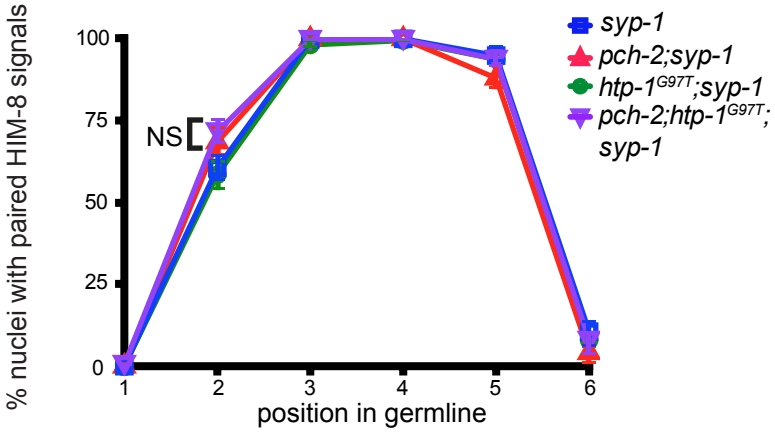

C

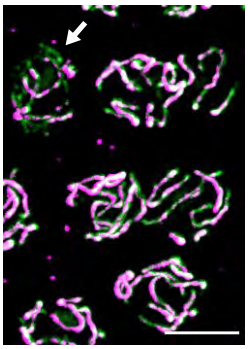

SYP-1
HTP-3

D

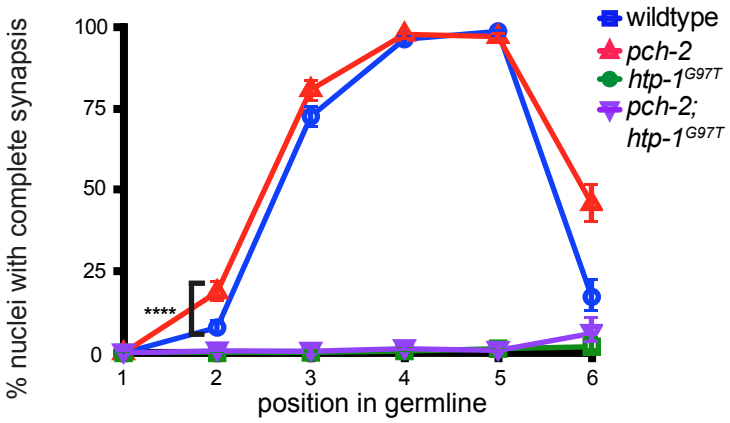

E

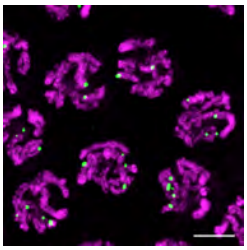

DNA
RAD-51

F

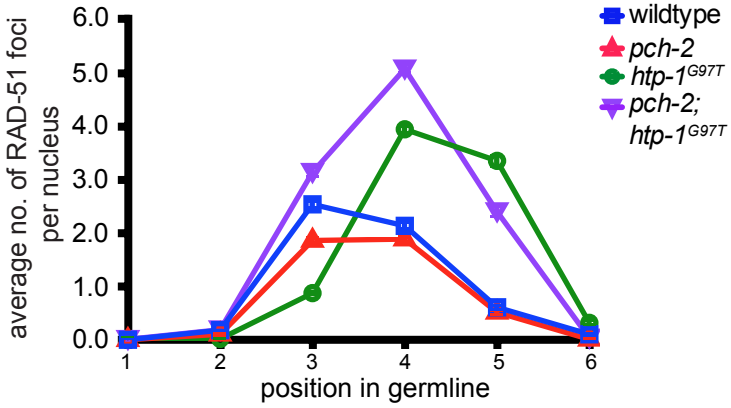

G

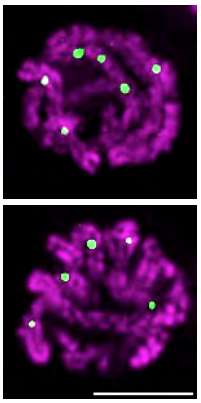

DNA
GFP::COSA-1

H

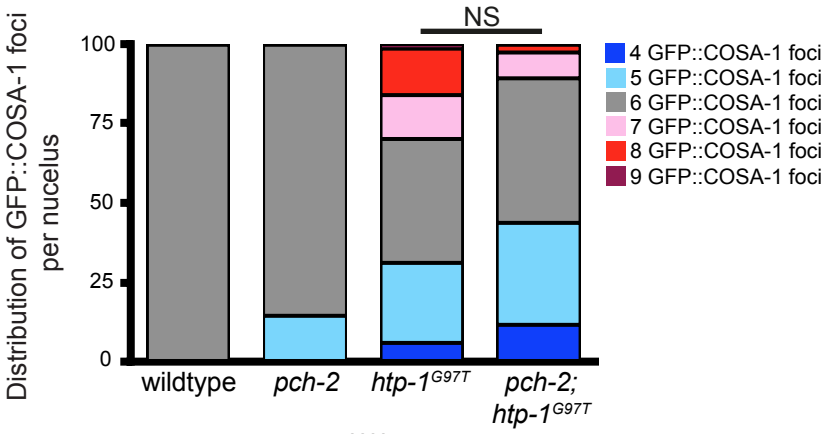

I

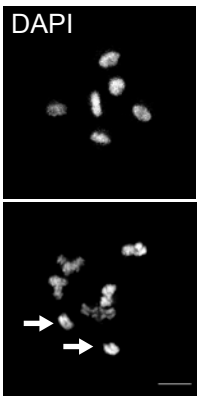

J

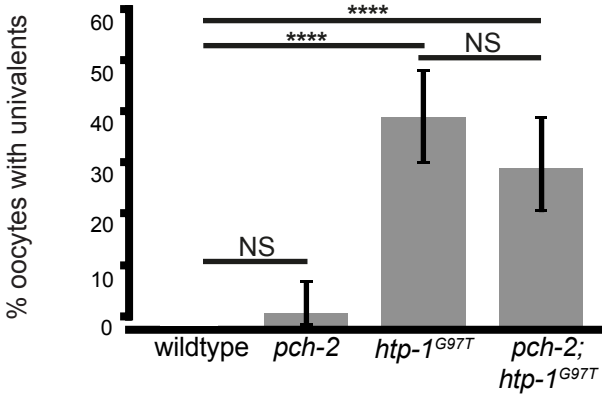

Figure 6

A

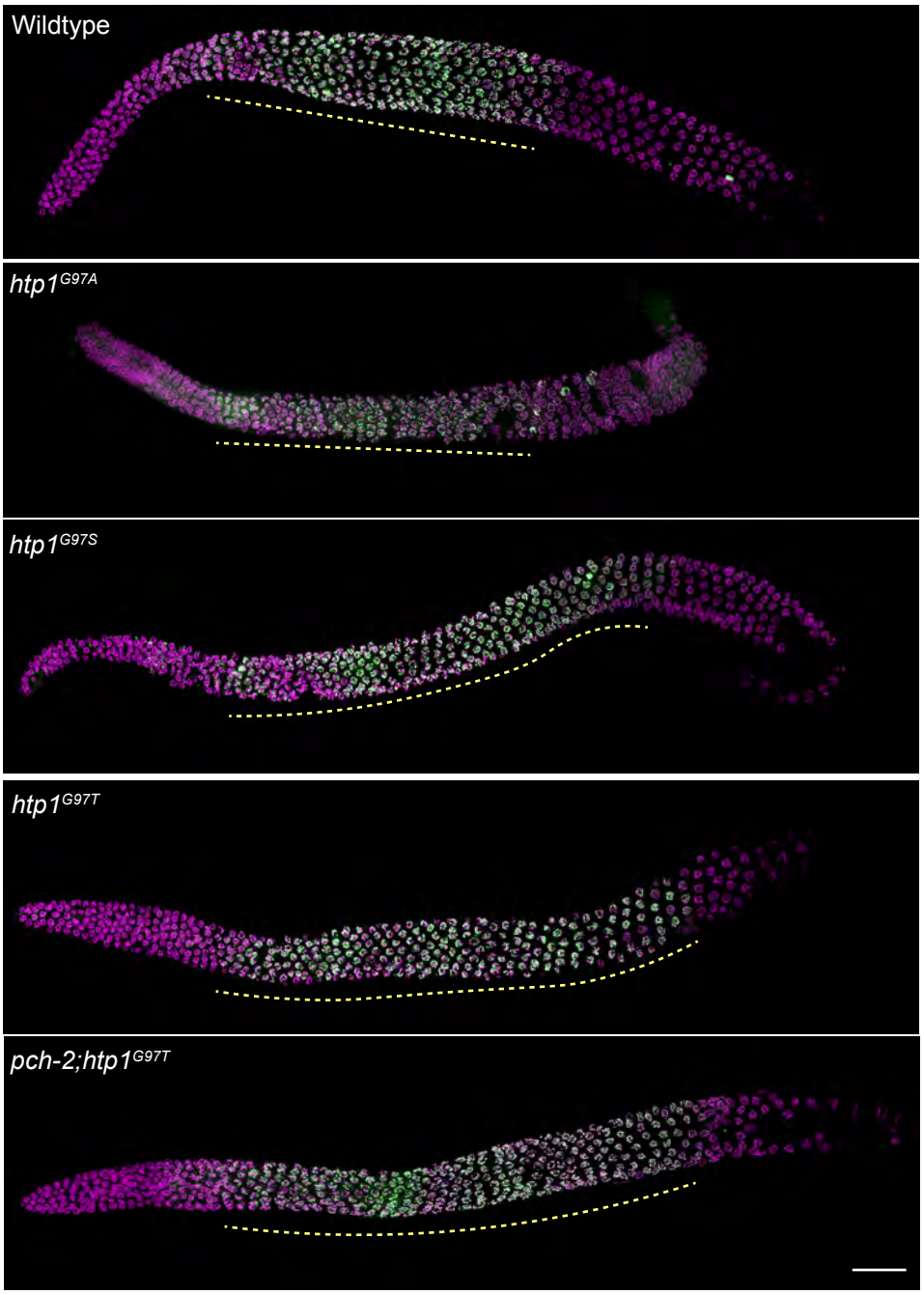
Wildtype
htp1G97A
htp1G97S
htp1G97T
pch-2;htp1G97T
DNA
DSB-1

B

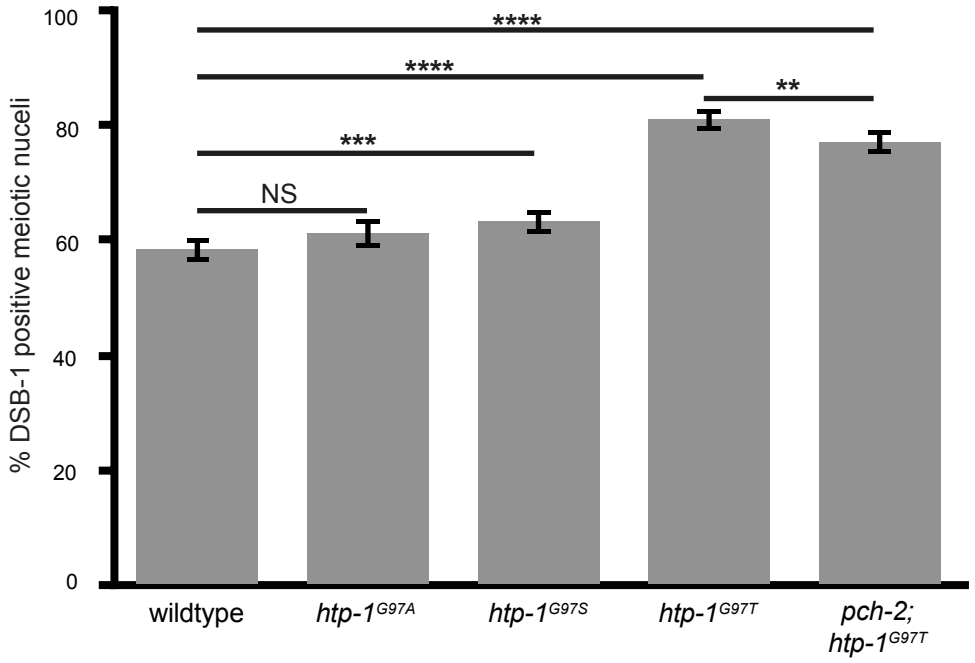
% DSB-1 positive meiotic nuceli
100
80
60
40
20
0
****
****
**
***
NS
wildtype
htp-1G97A
htp-1G97S
htp-1G97T
pch-2;
htp-1G97T

Figure 7

A

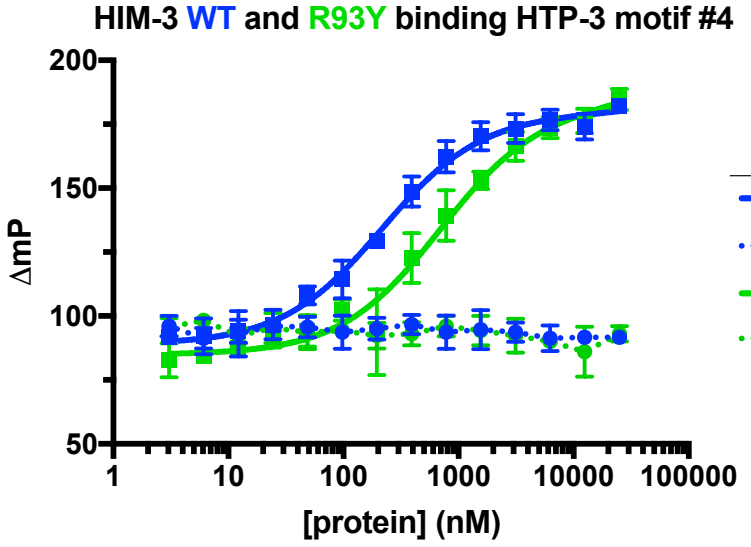

Protein	Peptide	*Kd*
HIM-3^{WT}	HTP-3 motif #4	220 +/- 20 nm
HIM-3^{WT}	Scrambled	*no binding*
HIM-3^{R93Y}	HTP-3 motif #4	690 +/- 130 nm
HIM-3^{R93Y}	Scrambled	*no binding*

B

Figure 8

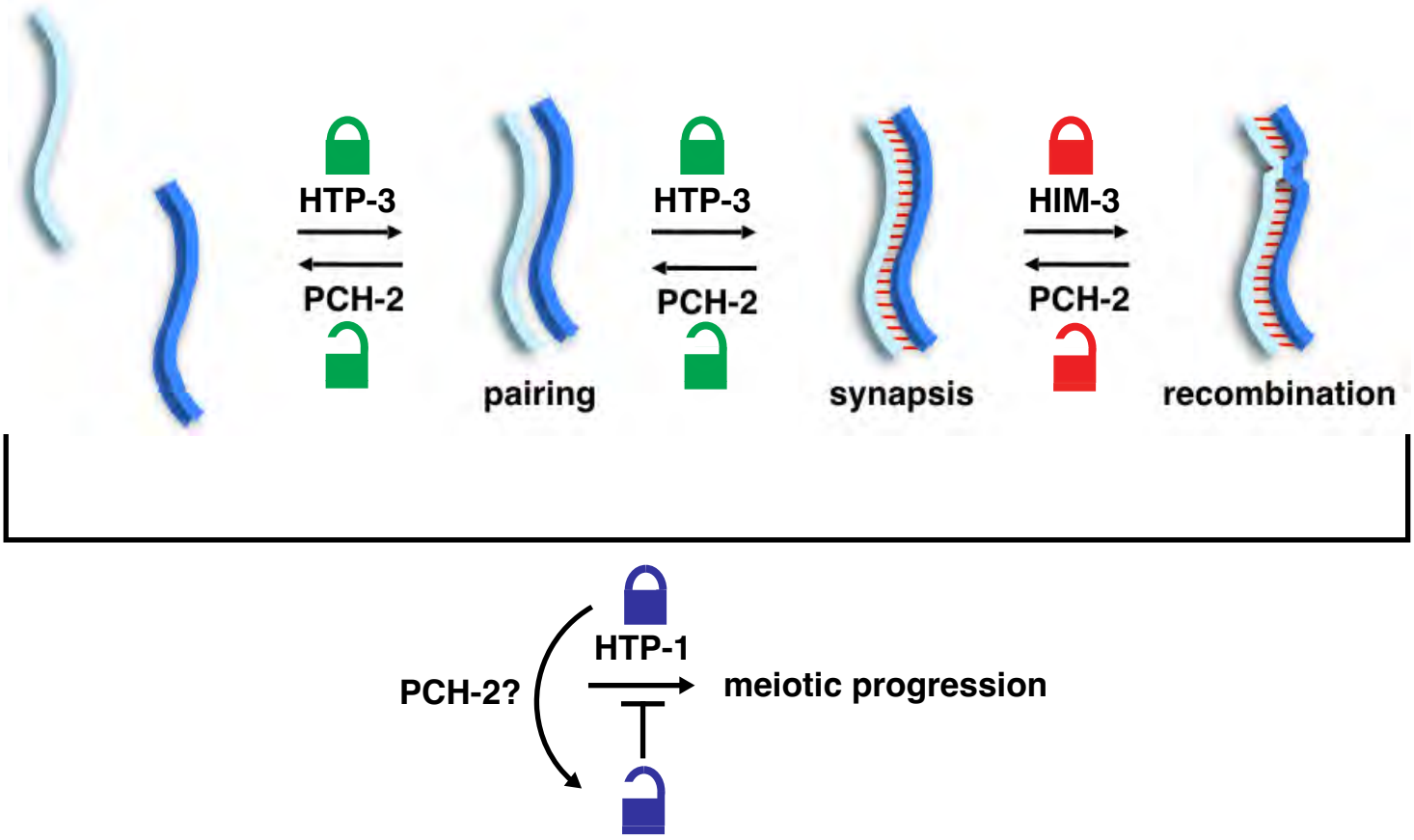
HTP-3
PCH-2
pairing
HTP-3
PCH-2
synapsis
HIM-3
PCH-2
recombination
HTP-1
PCH-2?
meiotic progression

Table S1. Data collection and refinement statistics

	HIM-3 R93Y
Data collection	
Synchrotron/Beamline	ALS 8.3.1
Date collected	9/14/2018
Resolution (Å)	63.4-1.3
Wavelength (Å)	1.11583
Space Group	$P6_1$
Unit Cell Dimensions (a, b, c) Å	73.23, 73.23, 110.82
Unit cell Angles (α,β,γ) °	90, 90, 120
I/σ (last shell)	27.4
[1]R_{sym} (last shell)	0.055 (2.245)
[2]R_{meas} (last shell)	0.056 (2.081)
[3]$CC_{1/2}$ (last shell)	1 (0.677)
Completeness (last shell) %	100 (100)
Number of reflections	1,632,957
unique	82,280
Multiplicity (last shell)	19.8 (19.7)
Refinement	
Resolution (Å)	63.4-1.3
No. of reflections	82274
working	4255
free	78019
[4]R_{work} (last shell) (%)	14.39 (31.35)
[4]R_{free} (last shell) (%)	16.39 (32.51)
Structure/Stereochemistry	
No. of atoms	4093
solvent	252
hydrogen	1907
r.m.s.d. bond lengths (Å)	0.021
r.m.s.d. bond angles (°)	1.58
Ramachandran favored/allowed (%)	97.03%/100%
Molprobity score	1.55
[5]SBGrid Data Bank ID	8CXK
[6]Protein Data Bank ID	910

[1] $R_{sym} = \sum\sum_j |I_j - \langle I \rangle| / \sum I_j$, where I_j is the intensity measurement for reflection j and $\langle I \rangle$ is the mean intensity for multiply recorded reflections.
[2] $R_{meas} = \sum_h [\sqrt{(n/(n-1))} \sum_j [I_{hj} - \langle I_h \rangle] / \sum_{hj} \langle I_h \rangle$, where I_{hj} is a single intensity measurement for reflection h, $\langle I_h \rangle$ is the average intensity measurement for multiply recorded reflections, and n is the number of observations of reflection h.
[3] $CC_{1/2}$ is the Pearson correlation coefficient between the average measured intensities of two randomly-assigned half-sets of the measurements of each unique reflection.
[4] R_{work}, $R_{free} = \sum||F_{obs}| - |F_{calc}||/|F_{obs}|$, where the working and free R-factors are calculated using the working and free reflection sets, respectively.

Figure S1

A

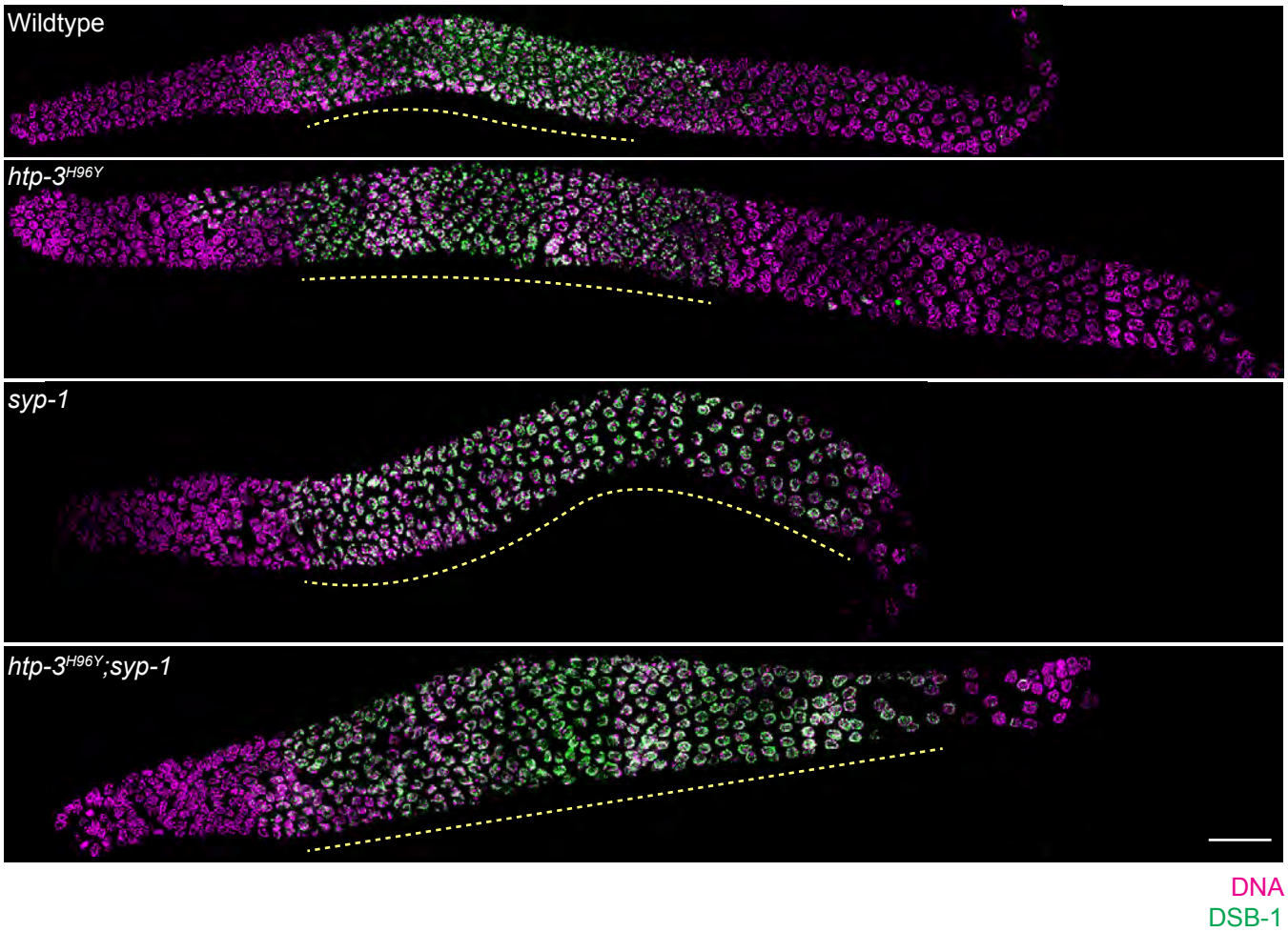

B

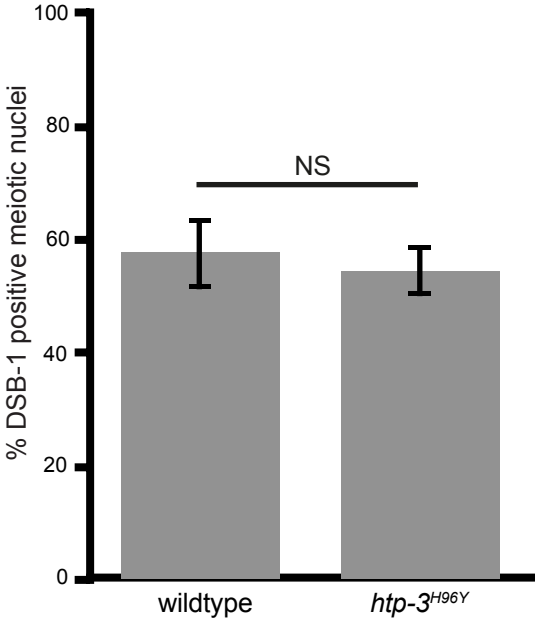

C

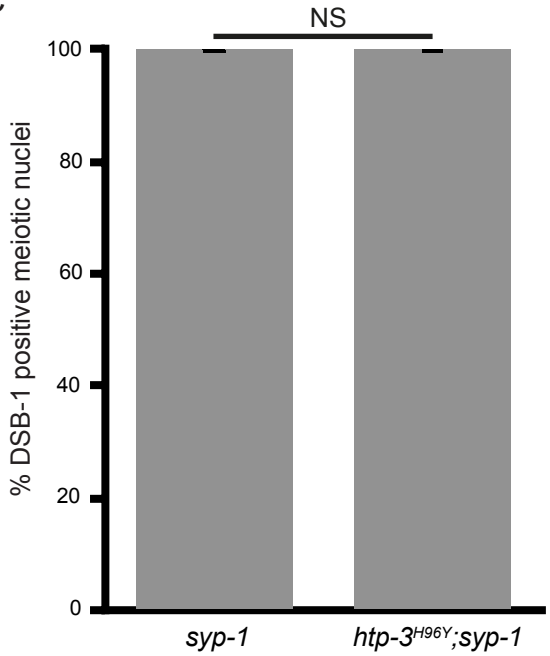

Figure S2

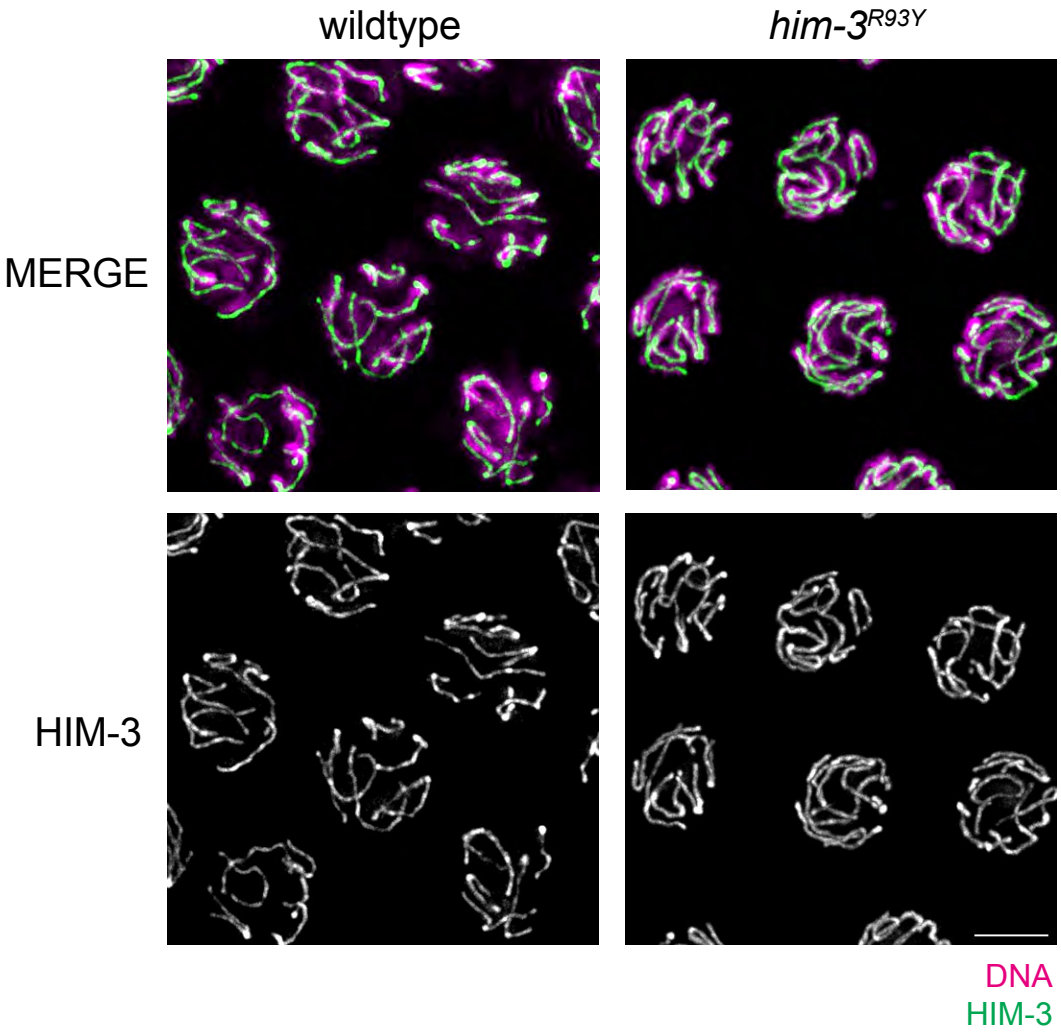

Figure S3

A

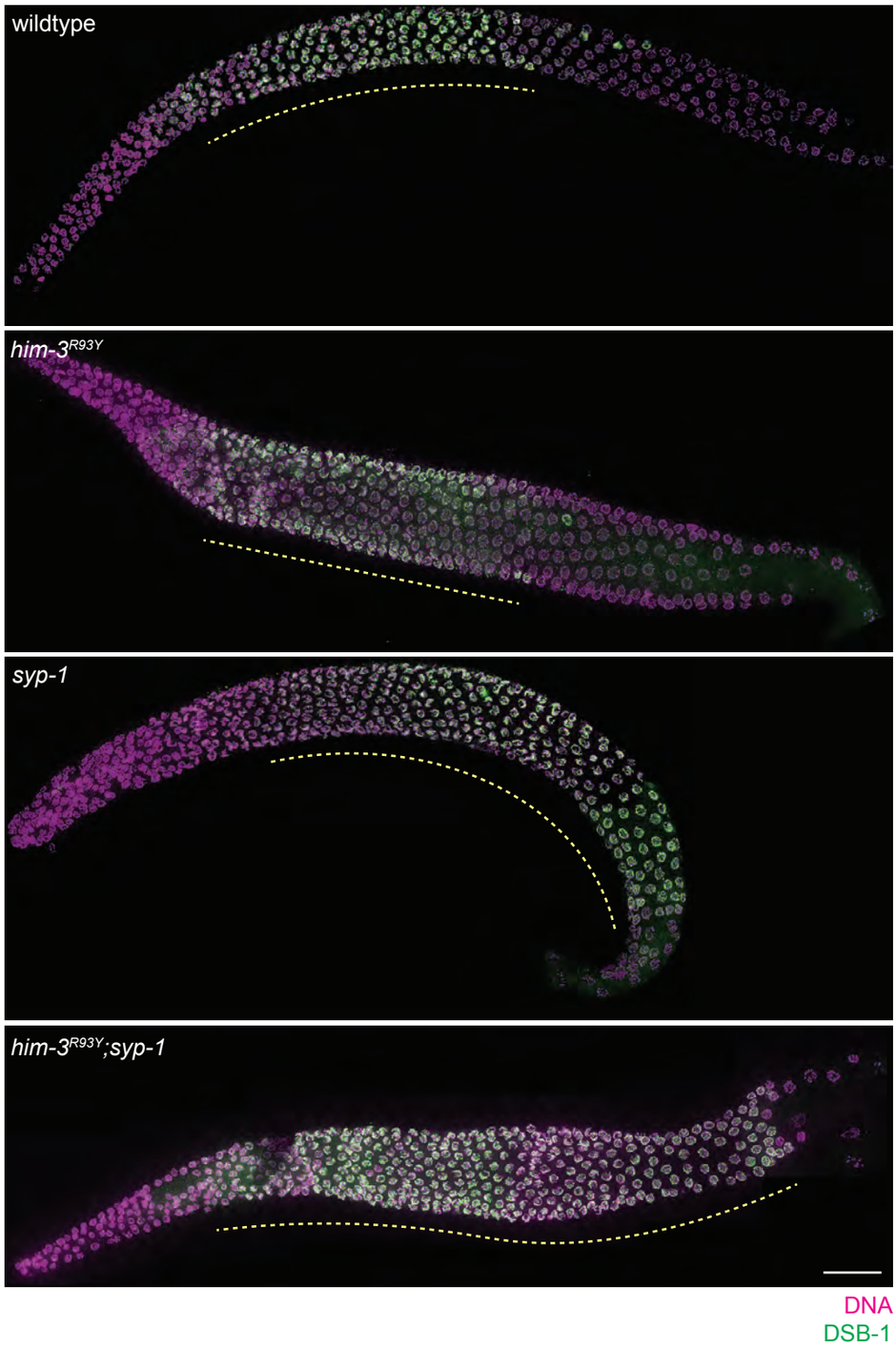

B

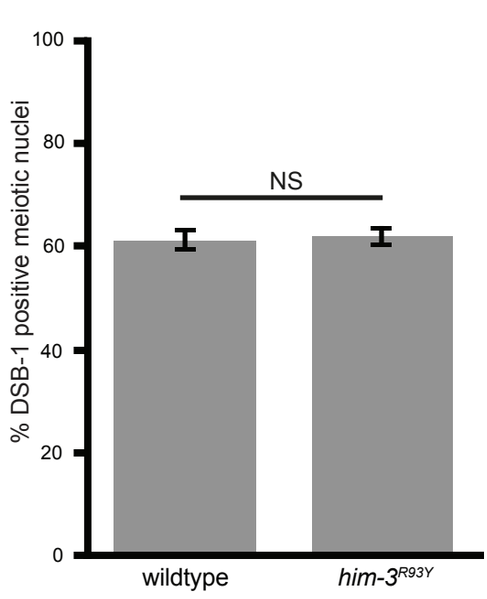

C

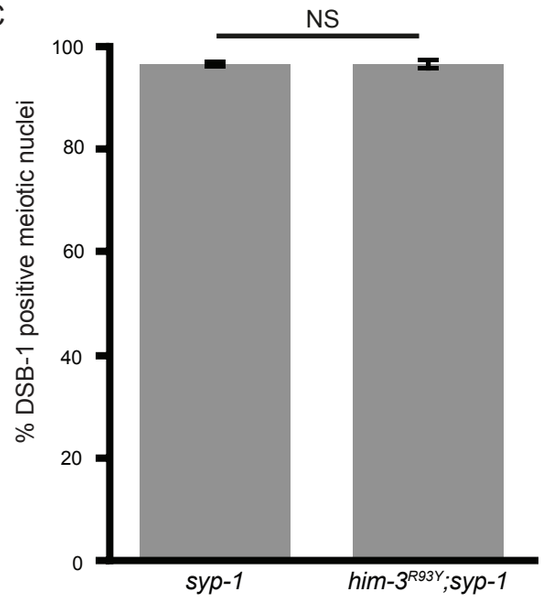

Figure S4

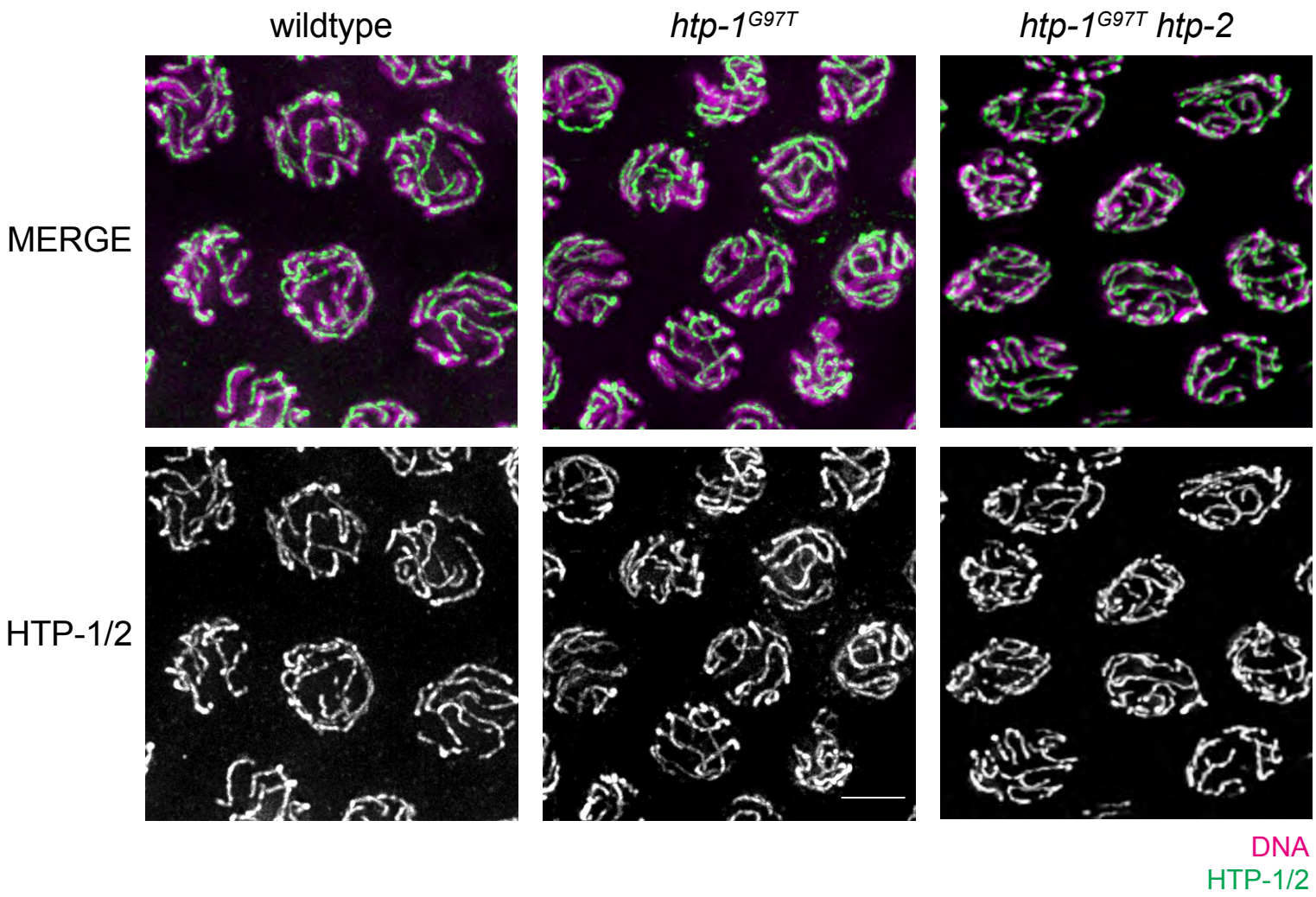

Figure S5

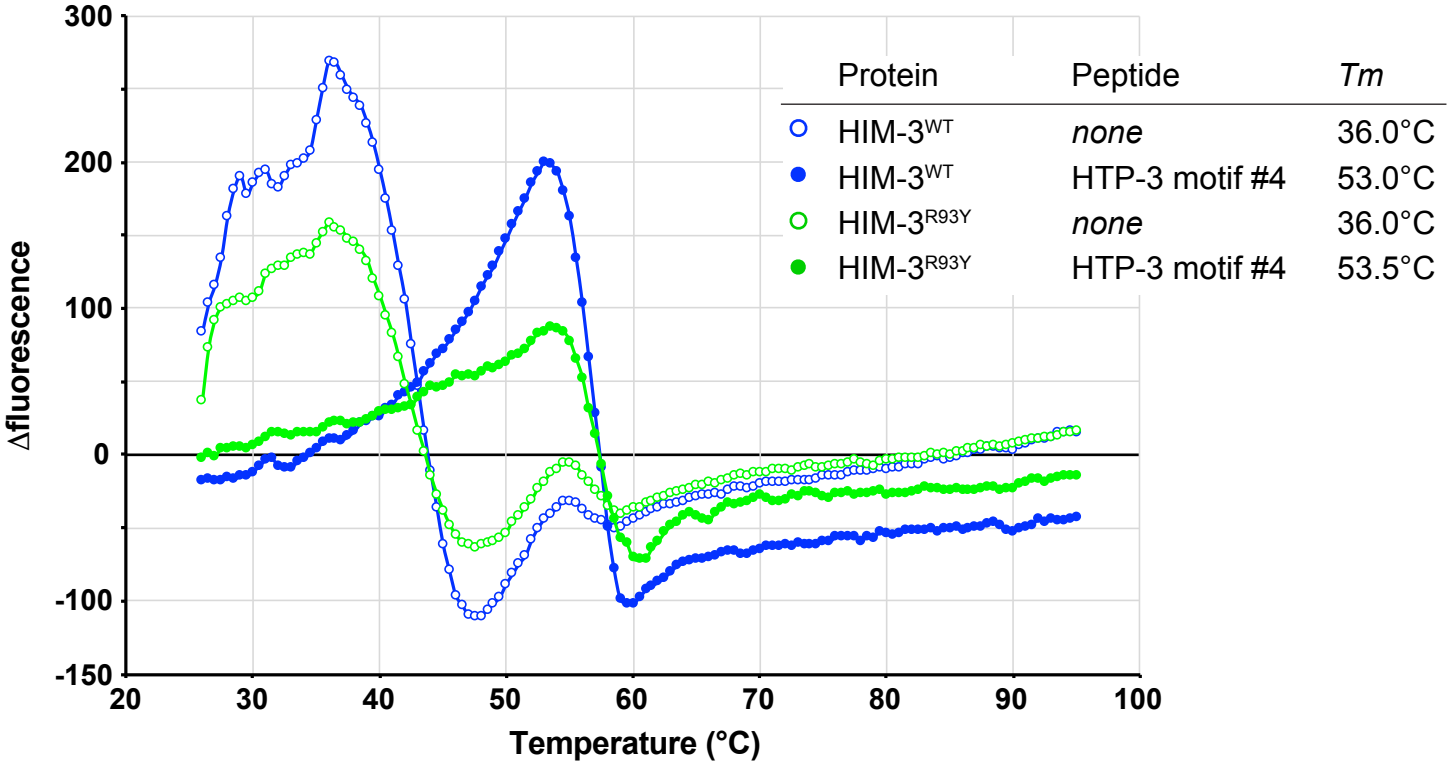
Protein
Peptide
Tm
HIM-3WT
none
36.0°C
HIM-3WT
HTP-3 motif #4
53.0°C
HIM-3R93Y
none
36.0°C
HIM-3R93Y
HTP-3 motif #4
53.5°C
Δfluorescence
Temperature (°C)
300
200
100
0
-100
-150
20
30
40
50
60
70
80
90
100

Figure S6

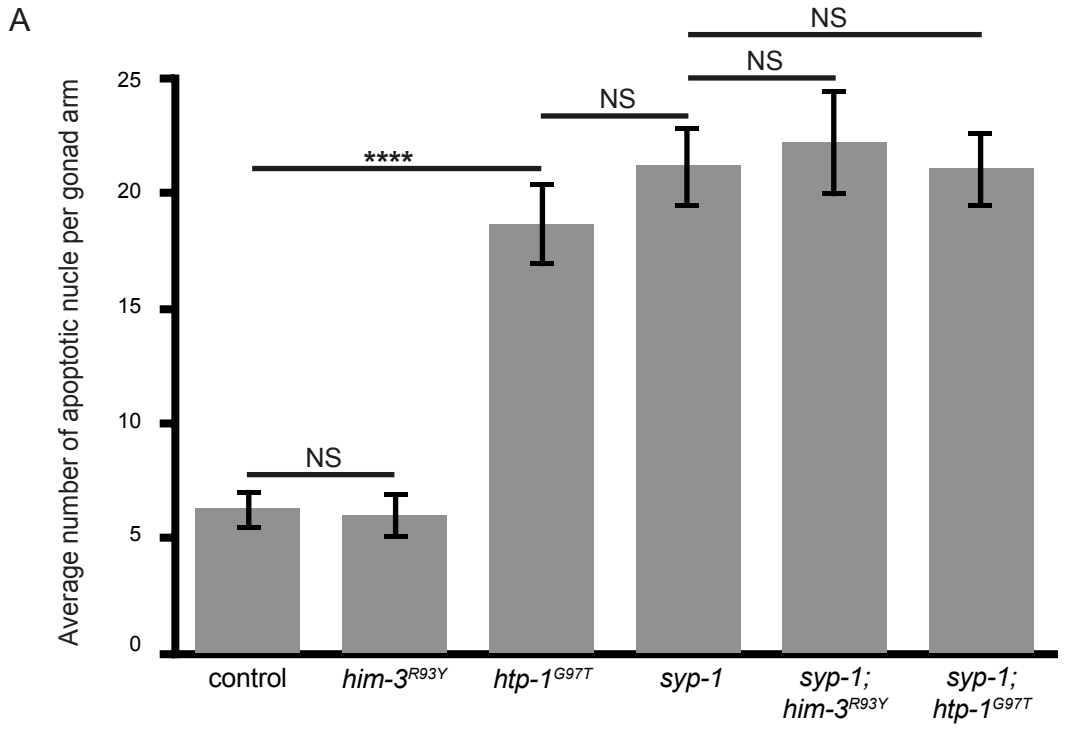
A
Average number of apoptotic nucle per gonad arm
25
20
15
10
5
0
****
NS
NS
NS
NS
control
him-3R93Y
htp-1G97T
syp-1
syp-1; him-3R93Y
syp-1; htp-1G97T